Partial-wave analysis of the reaction $\pi N \to \pi\pi N$ in the c.m energy range 1300–2000 MeV*

D. J. Herndon,† R. Longacre,‡ L. R. Miller, A. H. Rosenfeld, G. Smadja,‡ and P. Söding§
Lawrence Berkeley Laboratory, University of California, Berkeley, California 94720

R. J. Cashmore‖ and D. W. G. S. Leith
Stanford Linear Accelerator Center, Stanford University, Stanford, California 94305

(Received 4 November 1974)

A partial-wave analysis of the reaction $\pi N \to \pi\pi N$ has been carried out in the energy region 1300–2000 MeV. Two continuous solutions have been found; they are very similar in regions where data exist, but differ in the continuation of amplitudes through a gap between our low- and high-energy data. The second solution ("B") gives a much better fit to the data. These new partial-wave amplitudes provide important information on the inelastic couplings of the nucleon resonances to the $N\rho$, $N\epsilon$, and $\Delta\pi$ channels. A new resonance, $D_{13}(1700)$, long predicted by the quark model, has been observed coupling to two inelastic channels—ϵN and $\Delta\pi$, and the existence of a $P_{13}(1700)$ state is corroborated. Our preferred solution indicates a second new resonance, $P_{33}(1700)$, coupled strongly to the $\Delta\pi$ channel.

I. INTRODUCTION

Elastic phase-shift analyses have provided us with an impressive list of resonances, which is both the essence of our understanding of baryon spectroscopy and also the main testing ground for many of the ideas on the dynamics of hadronic processes. The agreement among the many independent groups is very impressive,[1-3] and gives confidence in the resulting scattering amplitudes.

Corresponding investigation of the inelastic scattering reactions has not kept pace with that of elastic reactions. This derives not only from the lack of data (with high statistics, and systematically spread in energy), but also from the complexity of the phenomenological analysis. However, the study merits the effort. As can be seen from Fig. 1, the inelastic cross section represents a very substantial fraction of the total πN cross section, even at 1.0 GeV/c, and it is therefore intrinsically interesting to understand the scattering process. In addition, the inelastic decays of N^* are a very specific signature of the state and its properties, and are therefore an important study in their own right. Finally, for resonances with very small coupling to the elastic channel [e.g., $D_{13}(1700)$] these studies are the only effective means of investigating the resonance in a formation experiment.

In the resonance region the principal inelastic reaction is

$$\pi N \to \pi\pi N . \tag{1.1}$$

We have therefore made a detailed study of this channel in the c.m. energy range 1300–2000 MeV.

In a previous analysis of these data in the range 1640–1760 MeV we attempted to isolate the reaction

$$\pi^- p \to \pi^+ \Delta^- \tag{1.2}$$

from

$$\pi^- p \to \pi^+ \pi^- n$$

by selecting only events with $1.14 < M(\pi^- n) < 1.320$.[4] This study enabled us to extract values for the F_{15}

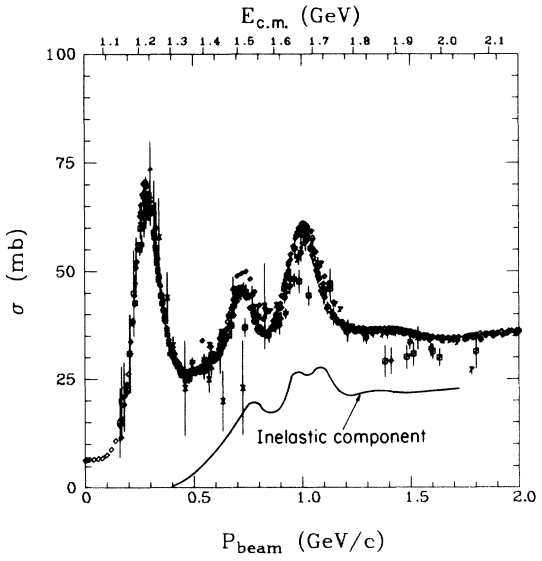

FIG. 1. Total and inelastic $\pi^- p$ cross section vs energy. The σ(inelastic) curve comes from Ref. 2 (EPSA) as in Eq. (4.21); the σ(tot) data come from Lovelace *et al.*, LBL Report No. 63 (unpublished).

and D_{15} coupling constants to the $\pi\Delta$ channel. Another group has used a similar technique to analyze[5] the reaction

$$\pi^+ p \to \pi^0 \Delta^{++} \tag{1.3}$$

to obtain the isospin-$\frac{3}{2}$ amplitudes in the c.m. energy range 1820–2090 MeV. (They have also contributed their data to the present study.)

In reactions of types (1.1) there is the possibility of producing many resonances which overlap strongly in the final states, particularly at lower c.m. energies. The interference effects associated with these overlaps are not removed by the Δ-selection techniques described above, and hence are an inherent limitation of such analyses. At higher energies the increased phase space and the possibility of using the mass conjugation technique[6] improve the situation. Nevertheless, the interference effects are still a problem. These effects led to fitting the reactions in their entirety using the isobar model and its extension[7]; these take into account the effects associated with many strong final-state interactions present. These methods have only been used currently at c.m. energies below 1560 MeV.[8-10]

We have extended this latter approach by including many more intermediate final states (and partial waves) and using the maximum-likelihood technique in confronting the data with theory. These extensions have allowed us to successfully apply this method throughout the energy range considered, 1300–2000 MeV. The data cover the regions 1300–1540 MeV and 1640–2000 MeV with a 100-MeV gap between the two regions. We presented one solution at the 1972 Batavia conference.[11] The energy-independent partial-wave analysis now yields two continuous solutions over the whole energy range. The solutions are very similar in the two regions where we have data, but have different continuations through the 100-MeV gap in the data. We favor solution B, but no fundamental ambiguity exists in the partial-wave analysis—when data in the gap region (1540–1640) become available, a clear choice between our two solutions will emerge. We include plots of our earlier solution A for historical reasons and also to demonstrate the stability of many of our conclusions concerning the partial-wave amplitudes. This analysis provides for the first time information on 50 inelastic couplings of the nucleon isobars and essentially accounts for all of the $\pi N \to \pi\pi N$ cross section in this energy range.

II. THE DATA

In the energy range we consider, single-pion production reactions can be unambiguously identified in the bubble chamber, resulting in effectively bias-free data. We have gathered data from several large bubble chamber experiments[8-10,12,13] leading to a total sample of 200 000 events covering the reactions

$$\pi^- p \to \pi^- \pi^0 p\,, \tag{2.1}$$

$$\pi^- p \to \pi^+ \pi^- n\,, \tag{2.2}$$

$$\pi^+ p \to \pi^+ \pi^0 p\,, \tag{2.3}$$

$$\pi^+ p \to \pi^+ \pi^+ n\,, \tag{2.4}$$

at energies 1300–2000 MeV. These experiments are listed in Table I.

The major features of reactions (2.1)–(2.3) can be observed in Figs. 2–5. The Dalitz plots of Figs. 2–4 demonstrate the presence of $\Delta(1236)$ production in all cases, although its contribution decreases at the higher energies. Indeed, at these higher energies the major final-state interaction is due to the ρ meson and its effects clearly should not be ignored even at the lower energies. The presence of these obvious resonance bands was the motivation for the quasi-two-body analyses of Refs. 4 and 5, but while the present solutions contain the qualitative features of Refs. 4 and 5,

TABLE I. Experiments used in this analysis.[a]

Beam particle	Laboratory (reference)	c.m. energy range (GeV) Low	High	Number of events	
				$\pi^+\pi^-n$	$\pi^-\pi^0p$
π^-	SLAC-LBL	1.47	1.50	1010	648
	(12)	1.64	1.97	41 175	27 946
	Oxford (10)	1.31	1.54	18 502	5892
	Saclay (8)	1.39	1.53	13 340	7314
	Total	1.31	1.97	74 027	41 800
				$\pi^+\pi^0p$	$\pi^+\pi^+n$
π^+	Oxford (9)	1.43	1.56	7262	1374
	Riverside-LBL (13)	1.82	2.09	41 412	17 255
	Saclay (8)	1.64	1.97	11 522	3382
	Total	1.43	2.09	60 196	22 011

[a] The events in this table, in the form of 16 full BCD Data Summary Tapes, are available on request. The π^+ events at or above $\sqrt{s} = 1820$ MeV must be requested from the UCR-LBL collaboration, care of Professor Anne Kernan, U. C. Riverside; the remainder from LBL, SLAC, or Saclay.

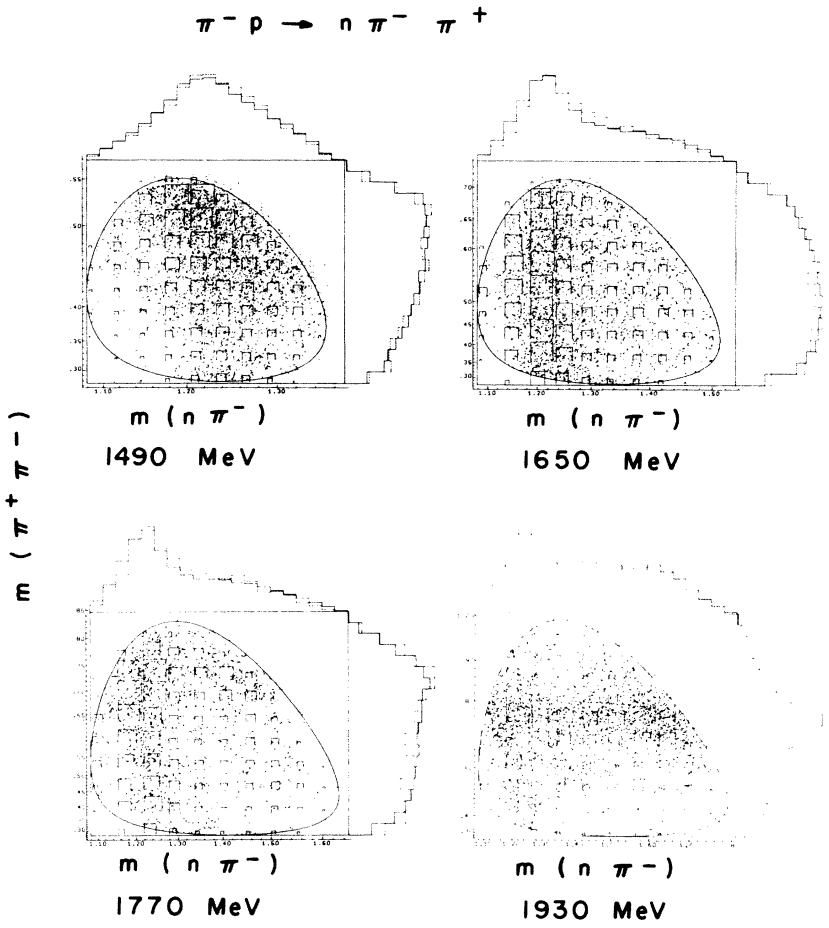

FIG. 2. Dalitz plots for the state $n\pi^-\pi^+$ at four c.m. energies: 1490, 1650, 1770, and 1930 MeV. The side of the little squares is proportional to the predicted density of our fits. On the projected distributions, the dotted line is the experimental data, while the solid histogram is the result of the fit. The scales are linear in (mass)^2, but the tiny numbers are actually in MeV.

they differ by many standard deviations from the earlier quantitative conclusions.

The variations in the structure of the production angle, θ, of the nucleon (see Fig. 5) are indicative of the presence of rapidly varying transition amplitudes. We can therefore anticipate that many partial waves will be necessary and that these will change rapidly with energy as expected from the presence of the structure in the inelastic cross sections of Fig. 1.

III. THE EXTENDED ISOBAR MODEL

In this section we summarize the ingredients of our extended isobar model and give the final formulas and partial waves we use in our fits. A detailed discussion and derivation of all formulas may be found in Herndon, Söding, and Cashmore.[14]

A. Ingredients of isobar model

(i) We assume that the reaction proceeds through three quasi-two-body channels,

$$\begin{aligned} \pi N &\to \pi\Delta(1236) \\ &\to N\rho(760) \\ &\to N\epsilon\,, \end{aligned} \tag{3.1}$$

where ϵ represents the strong s-wave $\pi\pi$ final-state interaction at around 650 MeV.

(ii) The reaction can proceed through a large number of partial waves. We then have a transition amplitude for each angular momentum and isospin state which we write as $T^c_{\alpha\mu}(\omega)$, where c represents the charge channel, e.g. $\pi^+\pi^- n$, $\pi^-\pi^0 p$, etc.; α is the group of quantum numbers (F, L, L', I, J) describing the reaction. These are

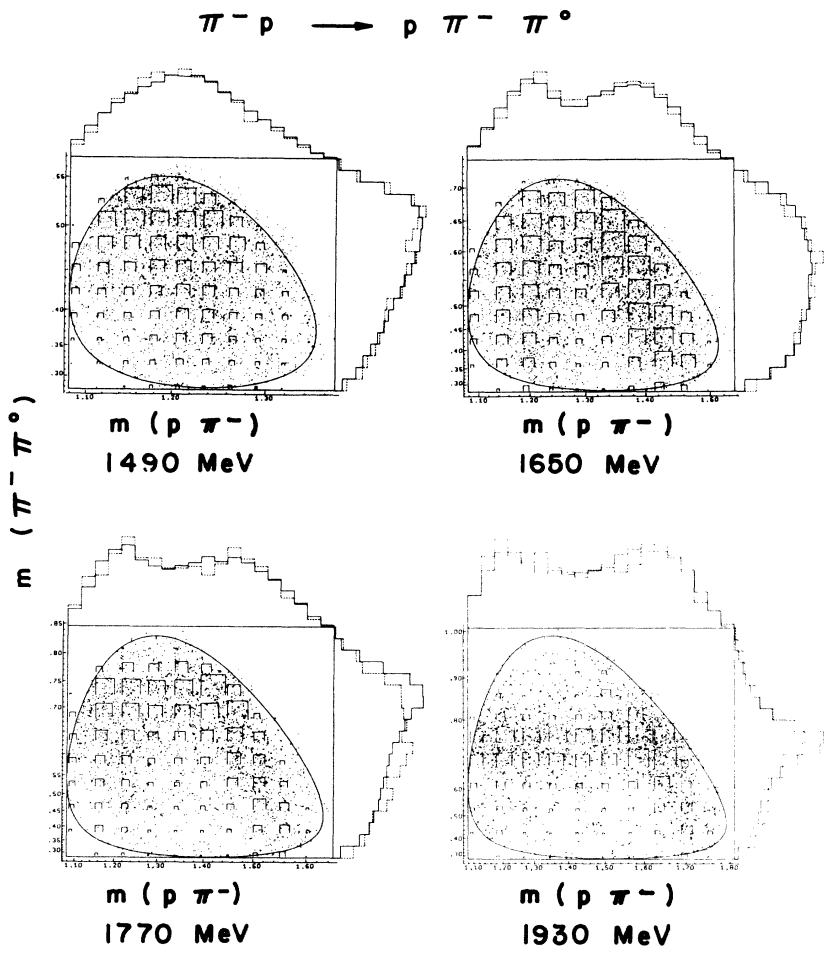

FIG. 3. Dalitz plot for the state $p\pi^-\pi^0$. For details see caption to Fig. 2.

summarized in Fig. 6, and the notation is spelled out below Eq. (3.2); μ represents μ_i, μ_f, the initial and final nucleon helicities; ω describes the four kinematical quantities necessary to describe an event: We choose these to be ω_1^2, ω_2^2—the Dalitz-plot variables—and $\cos\theta, \phi$—where θ, ϕ are the angles of the incident π in our final-state coordinate system.[14] Our z axis lies along the direction of the outgoing nucleon, and the y axis is perpendicular to the production plane. We note at this point that different charge channels differ only in isospin Clebsch-Gordan coefficients.

(iii) We can now explicitly develop some of the factors contained in $T^c_{\alpha\mu}(\omega)$:

$$T^c_{\alpha\mu}(\omega) = A_\alpha D_{\alpha\mu}(\omega) B_\alpha(\omega) W_F(\omega) C^c_\alpha \equiv A_\alpha X^c_{\alpha\mu}, \tag{3.2}$$

where $D_{\alpha\mu}(\omega)$ contains all spherical harmonic factors (D functions) associated with the angular momentum decomposition; $B_\alpha(\omega)$ contains the centrifugal barrier factor b_L, associated with the decay of the intermediate J^P state; $W_F(\omega)$ represents the Watson factor for the final-state interaction; A_α represents the amplitude for the particular wave and is assumed to be only dependent on the total mass of the system and not on any of the submasses. It is these complex parameters A_α which we vary during a fit; C^c_α the appropriate isospin Clebsch-Gordan coefficients for channel c.

(iv) The final transition amplitude to a given final state is then obtained by making a coherent sum of these individual amplitudes,

$$T^c_\mu(\omega) = \sum_\alpha T^c_{\alpha\mu}(\omega). \tag{3.3}$$

This summation implies some double counting of the amplitudes, which had been thought to be a small effect.[15] However, prompted by Aaron and Amado and others,[16] the Illinois group[17] and we are both estimating corrections to the ampli-

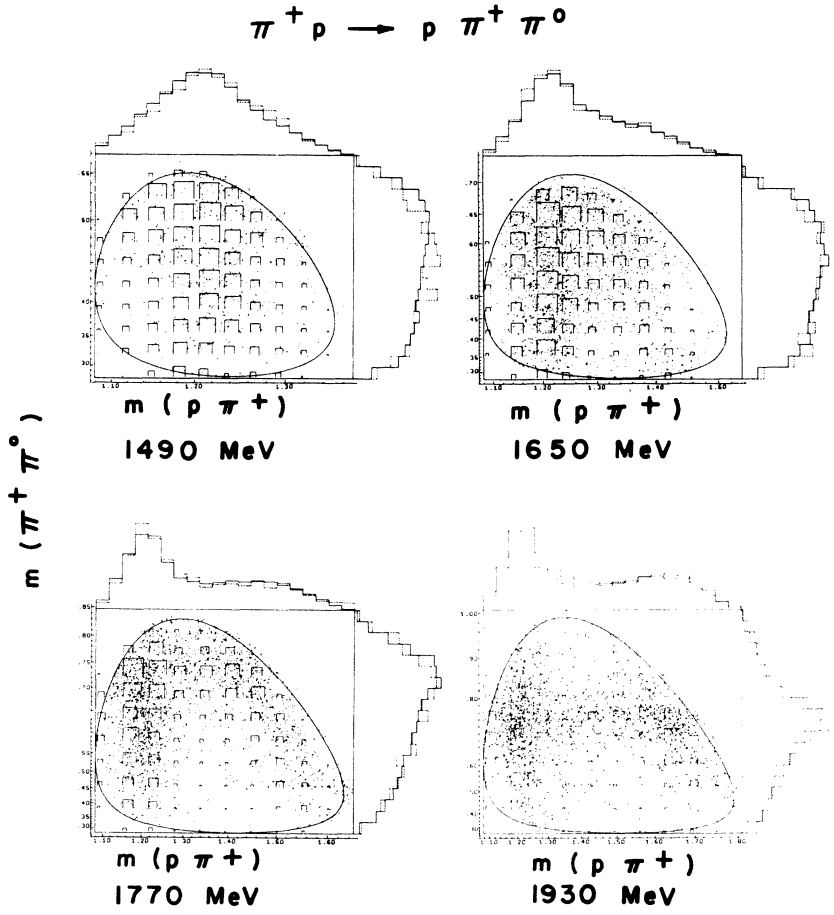

FIG. 4. Dalitz plot for the state $p\pi^+\pi^0$. For details see caption to Fig. 2.

tudes.[18]

(v) The differential cross section is then given by

$$d\sigma^c(\omega) = \lambda\!\!\!^{-2} \sum_\mu |T^c_\mu(\omega)|^2 , \tag{3.4}$$

where we sum over initial and final nucleon helicities, as we are neither working with polarized targets nor observing the final polarization.

This construction of the final-state amplitude and cross section allows easy fitting to all single-pion production channels and hence allows the partial-wave decomposition of the scattering amplitude.

(vi) Cross sections are expressed in terms of the conventional T-matrix elements T_α (called $T_{\pi N}$ for elastic scattering, $T_{\Delta\pi}$ for Δ production, etc.). The unitary circle has unit diameter, and if there were only a single channel present, the total cross section would be

$$\sigma_\alpha = 4\pi\lambda\!\!\!^{-2}(J+\tfrac{1}{2})|T_\alpha|^2 . \tag{3.5}$$

Note that by convention T carries no subscript μ as in Eq. (3.4); i.e.,

$$|T_\alpha|^2 = \int \sum_\mu |T_{\alpha\mu}|^2 d\Omega . \tag{3.6}$$

The nucleon helicity states are uniquely related by Clebsch-Gordan coefficients, i.e., $T_{\alpha\mu} \propto C(J, L', \mu) T_\alpha$, and so the actual amplitude T_α is well defined.

In practice, however, a single incoming partial wave can feed several values of α (i.e., several channels, such as $\pi\Delta, \rho N, \epsilon N$). This may result in substantial interference effects which are observable in the integrated cross section [see Eq. (3.7)]. The cross section is written as in (3.4),

$$\sigma_{\text{in}}(J^P) = \lambda\!\!\!^{-2} \int d\Omega \sum_\mu \left\{ \sum_\alpha |T_{\alpha\mu}|^2 + \text{interference terms} \right\},$$

which in the spirit of Eqs. (3.5) and (3.6) we define

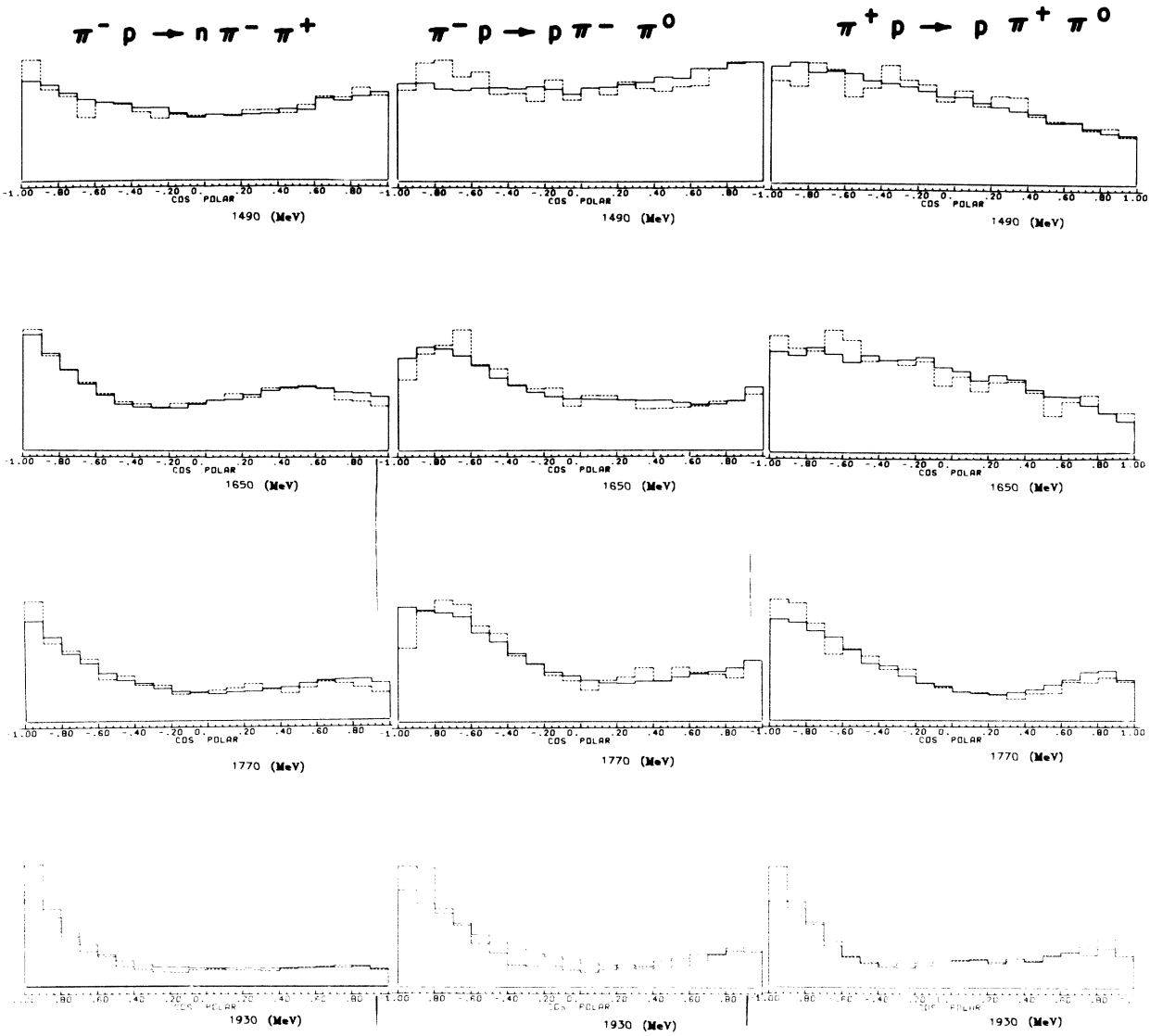

FIG. 5. Distribution of the angle of the final nucleon with respect to the incident pion in the center-of-mass system. The histograms are given at four c.m. energies: 1490, 1650, 1770, and 1930 MeV for the same channels as in Figs. 2–4. The dotted line is the data, the solid histogram the result of the fit.

as

$$\sigma_{\text{in}}(J^P) = 4\pi\lambda^2(J+\tfrac{1}{2})\left\{\sum_\alpha |T_\alpha|^2 + \text{overlap integrals}\right\}. \tag{3.7}$$

Equation (3.7) defines the normalization of the Argand plots. The overlap integrals are important and are taken into account at all stages of the program.

Different incoming partial waves never interfere, so we can write

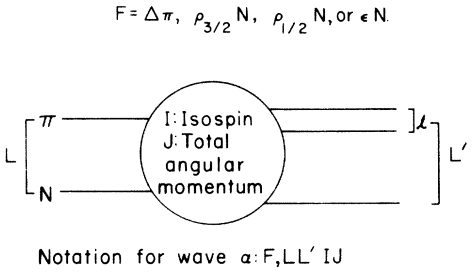

FIG. 6. Schematic representation of the isobar model and definition of the partial-wave notation. F describes the final-state particles, $\Delta\pi$, etc.

$$\sigma = \sum_{J^P} \sigma(J^P) . \tag{3.8}$$

B. The final-state interaction, W_F

This could be parametrized as a Breit-Wigner factor. However, rather than attempting to represent the Δ, ρ, or ϵ by Breit-Wigner forms we chose to use the Watson final-state interaction to describe the effects of these strong interactions by a factor

$$W_F = \frac{e^{i\delta_F} \sin\delta_F}{q^{l+1}} . \tag{3.9}$$

Here δ_F is the appropriate elastic phase for the strongly interacting particles, and q is the momentum of each particle in the isobar rest frame.

The actual values of δ_F are summarized in Fig. 7. The only uncertain phase shift was for the ϵ diparticle, but our parametrization is in close agreement with recent analyses[19] except near 1000 MeV, which fortunately is at the extreme limit of phase space for our highest beam energy. For more discussion, see Herndon.[20]

C. The centrifugal barrier, $b_{L'}$

We should include centrifugal barriers in both the incident state and the quasi-two-body intermediate state. However, the first of these is constant for a given partial wave at a given energy and hence we have ignored it. (Its inclusion would just result in a rescaling of A_α, which is unimportant—see below.)

The barrier factor in the intermediate state has been introduced as

$$b_{L'} = Q^{L'} , \tag{3.10}$$

where Q is the isobar momentum in the c.m. and L' the orbital angular momentum. Equation (3.10) is only the low-QR limit of the standard Blatt-Weisskopf factor,[21] which we meant to use. We inadvertently started with (3.10) and caught the mistake only after it was inconvenient to change. In Appendix C we show that (3.10) is adequate for our purpose, but urge the use of the correct form for all future partial-wave analyses.

D. The partial waves used in our fits

As discussed above we only considered three final-state interactions in our analysis:

(i) the $\Delta(1236)$ (intermediate state $\pi\Delta$),
(ii) the $\rho(760)$ (intermediate state $N\rho$),
(iii) the ϵ (intermediate state $N\epsilon$).

Since our decomposition of the amplitude is essentially an LS representation [where $\vec{S}=\vec{S}$ (diparticle spin) $+\vec{S}$ (bachelor-particle spin)], in the case of the ρ meson we have two transition amplitudes. These are obtained because

$$|\vec{S}_\rho + \vec{S}_N| = \tfrac{1}{2} \text{ or } \tfrac{3}{2} , \tag{3.11}$$

and are denoted as ρ_1 or ρ_3 waves.

In order to make the fitting problem tractable we have limited ourselves to orbital angular momenta in the incident and final states, L, $L' \leq 3$ and total angular momentum to $J \leq \frac{7}{2}$. In Table II we list the 60 waves with which we began the analysis. As described in the later sections the actual number of waves required increased with c.m. energy; the maximum was 28 at our higher energies.

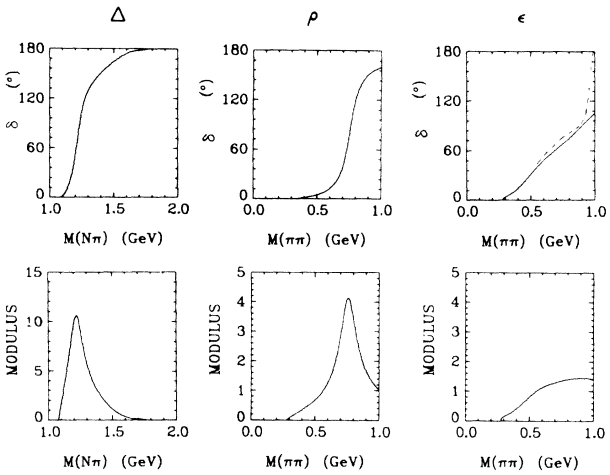

FIG. 7. Phase shifts and modulus of Watson factor $|W| = \sin\delta / q^{l+1}$ for Δ, ρ, and ϵ diparticles. Dashed line on the ϵ plot corresponds to the later analysis of Protopopescu (Ref. 19); all phase shifts used are given in Herndon's thesis (Ref. 20).

IV. THE FITTING PROGRAMS

A. Choice of method

The choice of fitting procedure is clearly dictated by the number of events available in a given experiment. To exploit the correlations that exist in the data in the case of limited statistics the most powerful approach is that of the maximum-likelihood technique.[22]

At the time we began our analysis, none of the existing maximum-likelihood fitting programs could handle either the amount of data or the number of parameters (up to 120) in a reasonable amount of computer time, so we developed a new program (RUMBLE)[23] which handles any problem in which the parameters appear bilinearly in the probability density (see below). It took the equivalent of 400 hours on the CDC 7600 to perform the

analysis described in this paper, including random starts, studies of uniqueness, etc.

B. Likelihood formulation

1. Likelihood in each charge channel

The full expression of $d\sigma^c/d^4\omega$ (in charge channel c) in terms of the search parameters, A_α, is given by (3.2) through (3.4) as

$$\frac{d\sigma^c}{d^4\omega}(\omega_i) = \lambda^2 \sum_\alpha |T_{\alpha\mu}|^2 ,$$
$$\frac{d\sigma^c}{d^4\omega}(\omega_i) = \lambda^2 \sum_\mu \left| \sum_\alpha A_\alpha X^c_{\alpha\mu}(\omega_i) \right|^2 . \tag{4.1}$$

For this formulation we rewrite $d\sigma/d^4\omega$ as $p(A_\alpha)$ to emphasize that it is a cross section predicted by the A_α, i.e.,

$$p^c(\omega_i, A_\alpha) = \lambda^2 \sum_\mu \left| \sum_\alpha A_\alpha X^c_{\alpha\mu}(\omega_i) \right|^2 . \tag{4.2}$$

We write the predicted *total* cross sections as

$$R^c(A_\alpha) = \int d^4\omega \, p^c(\omega_i) . \tag{4.3}$$

The normalized probability for each event is then

$$P(\omega_i, A_\alpha) = \frac{p^c(\omega_i, A_\alpha)}{R^c(A_\alpha)}, \tag{4.4}$$

and the likelihood L^c describing the *shape* of the distribution is

$$L^c_{\text{shape}}(\omega_i, A_\alpha) = \prod_{i=1}^{N^c} p^c = \frac{1}{(R^c)^{N^c}} \prod_{i=1}^{N^c} p^c(\omega_i, A_\alpha) . \tag{4.5}$$

If we dealt with only *one* charge channel, common sense would tell us to adjust the scale of the A_α by setting $R^c(A_\alpha)$ equal to the measured channel cross section σ^c, but for several channels the correct scaling is more complicated. Hence we must next formulate the generalized likelihood L^c more precisely.

The pathlength l^c may differ from channel to channel. If each experiment reports N^c events and a cross section σ^c, then

$$l^c = \frac{N^c}{\sigma^c} (\text{events}/\mu\text{b}) , \tag{4.6}$$

and the predicted number of events ν^c is given by

$$\nu^c = l^c R^c(A_\alpha) = \frac{N^c}{\sigma^c} R^c(A_\alpha) . \tag{4.7}$$

The Poisson probability of observing ν events when N are expected is

$$P(\nu, N) = \frac{\nu^N e^{-\nu}}{N!} . \tag{4.8}$$

TABLE II. The 60 waves with angular momenta L, L', l each ≤ 3. There are two nucleon-ρ terms in the isobar model, indicated by ρ_3 and ρ_1, where the subscript indicates the coupling between the spin of the ρ ($l=1$) and the spin of the outgoing nucleon. See Fig. 6 for more complete explanation of the notation. We never needed more than 28 of these 60 waves.

Isospin	Incident wave	$\pi\Delta$	$N\rho_3$	$N\rho_1$	$N\epsilon$
$I=\frac{1}{2}$	S_{11}	SD_{11}	SD_{11}	SS_{11}	SP_{11}
	P_{11}	PP_{11}	PP_{11}	PP_{11}	PS_{11}
	D_{13}	DS_{13} DD_{13}	DS_{13} DD_{13}	DD_{13}	DP_{13}
	P_{13}	PP_{13} PF_{13}	PP_{13} PF_{13}	PP_{13}	PD_{13}
	D_{15}	DD_{15}	DD_{15}	DD_{15}	DF_{15}
	F_{15}	FP_{15} FF_{15}	FP_{15} FF_{15}	FF_{15}	FD_{15}
	F_{17}	FF_{17}	FF_{17}	FF_{17}	
$I=\frac{3}{2}$	S_{13}	SD_{31}	SD_{31}	SS_{31}	
	P_{31}	PP_{31}	PP_{31}	PP_{31}	
	D_{33}	DS_{33} DD_{33}	DS_{33} DD_{33}	DD_{33}	
	P_{33}	PP_{33} PF_{33}	PP_{33} PF_{33}	PP_{33}	
	D_{35}	DD_{35}	DD_{35}	DD_{35}	
	F_{35}	FP_{35} FF_{35}	FP_{35} FF_{35}	FF_{35}	
	F_{37}	FF_{37}	FF_{37}	FF_{37}	

Using (4.7) this becomes $P(\nu, N) = (1/N!)(N/\sigma)^N R^N e^{-NR/\sigma}$, i.e., inserting the superscript c,

$$P(\nu^c, N^c) = \frac{1}{N^c!} \left(\frac{N^c}{\sigma^c}\right)^{N^c} (R^c)^{N^c} e^{-N^c R^c/\sigma^c} . \tag{4.9}$$

We now form the generalized channel likelihood,[24] $L^c = P(\nu^c, N^c) L^c_{\text{shape}}$, where P is given by (4.9) and L^c_{shape} by (4.5). The R^c factors cancel to give

$$L^c = \frac{(N^c/\sigma^c)^{N^c}}{N^c!} \exp\left\{-\frac{N^c R^c}{\sigma^c}\right\} \prod_1^{N^c} p^c(\omega_i, A_\alpha) . \tag{4.10}$$

Finally the multichannel likelihood L is the product of each L^c,

$$L = \prod_c \left[\frac{(N^c/\sigma^c)^{N^c}}{N^c!}\right] \exp\left\{-\frac{N^c R^c}{\sigma^c}\right\} \prod_1^{N^c} p^c(\omega_i, A_\alpha) . \tag{4.11}$$

2. Analytic scaling of the A_α

We have already said that if we had only one charge channel we could set $R^c = \sigma^c$. Let us check this for single channel Eq. (4.10) by introducing a scale factor, s, e.g.

$$A_\alpha = sA_\alpha^0 . \tag{4.12}$$

Dropping factors which do not contain s, Eq. (4.10) becomes

$$L^c(sA_\alpha^0) = \exp\left\{-\frac{N^c s^2 R^c(A_\alpha^0)}{\sigma^c}\right\} (s^2)^{N^c} \prod_1^{N^c} p^c(\omega_i, A_\alpha^0) , \tag{4.13}$$

$$\ln L^c(sA_\alpha^0) = -\frac{N^c s^2 R^c(A_\alpha^0)}{\sigma^c} + N^c \ln s^2 + \text{constant} , \tag{4.14}$$

$$\frac{\partial \ln L^c(sA_\alpha^0)}{\partial s} = -\frac{2N^c s R^c(A_\alpha^0)}{\sigma^c} + 2N^c \frac{1}{s} . \tag{4.15}$$

Setting this to zero gives

$$\frac{1}{s^2} = \frac{R^c(A_\alpha^0)}{\sigma^c} , \tag{4.16}$$

which as we guessed earlier indeed gives

$$R^c(A_\alpha) = s^2 R^c(A_\alpha^0) = \sigma^c$$

and

$$L^c(s^{\max} A_\alpha^0) = e^{-N^c}\left[\frac{\sigma^c}{R^c(A_\alpha^0)}\right]^{N^c} \prod_1^{N^c} p^c(\omega_i, A_\alpha^0) . \tag{4.17}$$

This expression is manifestly independent of the magnitude of the vector A_α^0.

Next we can apply the same procedure to the multichannel L of Eq. (4.11). Details are given in Appendix A. This time the equivalent of (4.16) is easily found to be

$$s^2|_{L_{\max}} \equiv s^2 = \frac{N}{\sum R^c N^c/\sigma^c} , \tag{4.18}$$

where $N \equiv \sum N^c$.

It is also shown in Appendix A that inserting this into (4.11) yields a multichannel likelihood

$$L(s_{\max} A_\alpha) = Be^{-N} N^N \left[\sum \frac{N^c R^c(A_\alpha)}{\sigma^c}\right]^{-N} \times \prod_c \prod_{i=1}^{N^c} p^c(\omega_i, A_\alpha) . \tag{4.19}$$

The quantity which we actually maximize is the average logarithm of (4.19) premaximized with respect to the scale of A_α.

$$F = \frac{1}{N}\ln L = \text{constant} - \ln\left[\sum_c \frac{N^c R^c(A_\alpha)}{\sigma^c}\right] + \frac{1}{N}\sum_c \sum_{i=1}^{N^c} \ln p(\omega_i, A_\alpha) . \tag{4.20}$$

C. Unitarity and the agreement with elastic phase-shift predictions

Using unitarity and the elastic amplitude from elastic partial-wave ("phase-shift") analysis (EPSA), one gets upper bounds for $\sigma(N\pi\pi, IJ^P)$. The partial waves used were those available in 1970, when we started this analysis.[20] For most of our fits we did not need (or impose) these constraints. Even in those cases in which we predicted more cross section than allowed, we were within two standard deviations of the upper bound. To correct this, we added to $F(A_\alpha)$ the χ^2-like terms F_{EPSA},

$$F_{\text{EPSA}} = -\frac{1}{N}\sum_{IJP} \alpha_{IJP}\left[\frac{\sigma^{IJP} - \sigma^{IJP}_{\text{EPSA}}}{\delta\sigma^{IJP}_{\text{EPSA}}}\right]^2 \theta(\sigma^{IJP} - \sigma^{IJP}_{\text{EPSA}}) , \tag{4.21}$$

where σ^{IJP} is defined by (3.7) and $\sigma^{IJP}_{\text{EPSA}}$ is an average over the different EPSA, and $\delta\sigma^{IJP}_{\text{EPSA}}$ are the external errors on $\sigma^{IJP}_{\text{EPSA}}$. By using the step function, θ, F_{EPSA} only affected the likelihood when the fitting parameters predicted *more* cross section than allowed. These additional terms had very little effect on the fitted parameters. Of those amplitudes affected, the modulus was slightly reduced but the phases never changed.

D. Stepping to a maximum

Maximizing procedures are of three general categories. At each step they evaluate

(i) only the function F, or

(ii) F and the first derivative vector ∇F, or

(iii) F, ∇F, and the second derivative matrix, $\nabla\nabla^T F$ (the superscript T means transpose). For convenience we define the variance matrix $\underline{V} = (\nabla\nabla^T F)^{-1}$.

We have found that the most efficient fitting technique is a combination of types (ii) and (iii).

In both types of fitting programs, one "step" in the parameters is given by $\Delta\vec{A} = -\underline{V}' \cdot \nabla F$ where $\underline{V}'$ is a negative-definite approximation to $\underline{V}$ (for some cases $\underline{V}' = \underline{V}$). We use two methods of updating $\underline{V}'$, the Davidon method[25] and a modified form of the Newton-Raphson method.[26]

1. The Davidon method

The Davidon method belongs to category (ii). The initial $\underline{V'} = \underline{V'_1}$ is chosen to be diagonal, and at each subsequent step $\underline{V'_1}$ is modified by the addition of a rank-one matrix. A rank-one matrix is one having just one eigenvector with a nonzero eigenvalue. A typical example is the outer product of a vector with itself, $M_{ij} = v_i v_j$ or in matrix notation $\underline{M} = \vec{v}\vec{v}^T$. If $\vec{v}$ has unit magnitude, then $\underline{M}$ is called a projector. Davidon showed that at the ith step $\underline{v'}$ should be modified by

$$\underline{V'_{i+1}} = \underline{V'_i} + \lambda[\underline{V'_i} \cdot \nabla F_i][\underline{V'_i} \cdot \nabla F_i]^T . \tag{4.22}$$

The number λ is calculated from $\underline{V'_i}$, ∇F_i, and ∇F_{i-1}. To ensure that the step is toward a maximum, rather than a minimum or saddlepoint, λ is adjusted if necessary to keep $\underline{V'_i}$ negative-definite. This adjustment to V'_i reflects the additional knowledge about the curvature of F gained from knowing the new first derivative ∇F_i. If the $2n$-dimensional $\vec{A}$ space is quadratic, Davidon showed that after $2n$ steps $\underline{V'_{2n}} = \underline{V'}$.

2. The original Newton-Raphson method

This method chooses $\underline{V'} = \underline{V}$ and recalculates the entire matrix at each step. The modified method, which we use, calculates a negative-definite approximation to $\nabla\nabla^T F$ and takes $\underline{V'}$ to be the inverse of this approximate matrix. The approximation is such that if our model exactly predicts the event distribution for some vector $\vec{A}'$, then $\underline{V'} = \underline{V}$ at $\vec{A}'$.

3. Our procedure

Our fitting procedure was to calculate and invert the approximate second derivative matrix every twenty steps. In between these steps we used the Davidon technique to update the matrix. We also found it more efficient to take a few (in our case 5) Davidon-type steps initially before inverting the second derivative matrix.

4. Redundant parameters

Since F is invariant to scale changes in $\vec{A}$ and to an overall phase change in $\vec{A}$, there are two redundant parameters, and the second derivative matrix is singular. These singularities are usually eliminated in problems similar to ours by permanently freezing the phase and modulus of one A_α and reducing by two the dimension of $\nabla\nabla^T F$. We find, however, that the maximizing procedure takes less than one-third the number of steps to reach a maximum if *all* the A_α are permitted to vary. In this case, the second derivative matrix has two eigenvectors with zero eigenvalues. The desired $\underline{V'}$ is the inverse of $\nabla\nabla^T F$, restricted to the space spanned by the set of eigenvectors with nonzero eigenvalues. For details on how the fitting program calculates the proper $\underline{V'}$, see Ref. 23. A two-dimensional example is given in Appendix B.

E. Errors in amplitudes on Argand plots

The error matrix $\underline{E}$ is given by

$$\underline{E} = \langle \delta\vec{A} \cdot \delta\vec{A}^T \rangle = \frac{1}{N}\underline{V'} , \tag{4.23}$$

where $\underline{V'} \approx \nabla\nabla^T F$ as described above, and the factor $1/N$ arises because $\ln L = NF$.

In the neighborhood of any local maximum at $A^{\max}$ with likelihood $L^{\max}$, we can expand L as

$$L = L^{\max} \exp\{-\tfrac{1}{2}\chi^2\} , \tag{4.24}$$

and an error hyperellipsoid may be defined by a hypersurface in A space labeled by $\Delta\chi^2 = 1$, i.e., by $L = L^{\max} e^{-1/2}$.

To plot error ellipses on our Argand plots we project this hypersurface on the complex plane representing a single T_α (or A_α). However, the probability that a result will be within this ellipse is only 40%. In order to increase this probability we have conservatively doubled our estimated error, thereby raising the χ^2 contour to 4, and enclosing 87% of the probability. In summary, all the errors plotted or tabulated in this paper and in our previous publications are twice those calculated by the program RUMBLE which uses (4.23).

F. Relative likelihood of competing solutions

We were bound to encounter two different sorts of competing solutions:

(i) The number of parameters (waves) is the same for both solutions, as in the case where two starting values lead to competing maxima.

(ii) The number of parameters differs, as when we have cast out a wave from solution A with likelihood L_A, found a new maximum B, and wonder if the new L_B is significantly worse than L_A.

For the discussion below, assume that hypothesis A is the right one and that after a fit we find a likelihood ratio L_A/L_B which we call L_{AB}. A standard approach is then to say that solution B is ruled out to 3σ if $\ln L_{AB} = NF_{AB}$ is greater than 4.5 (or 2σ if $NF_{AB} > 2$). We now carry this test one step further and take into account the error δF_{AB} in F_{AB}. Specifically we wish not to eliminate solution B unless $F_{AB}/\delta F_{AB}$ is safely larger than unity. (More sophisticated versions of this test are discussed by Eberhard, Rosenfeld, and Tabak.[27]) We apply the same numerical test to both sorts of competing solutions (i) and (ii) mentioned above.

Of course without generating Monte Carlo events we do not know δNF_{AB}, but we can *estimate* it from

the 10 000 events in hand at each energy. For each event i we form F^i_{AB} and can then evaluate

$$(\delta' F_{AB})^2 = \frac{\sum (F^i_{AB})^2}{N} - \left(\frac{\sum F^i_{AB}}{N}\right)^2 . \qquad (4.25)$$

Figure 8 is a scatter plot of typical values of $\delta' F_{AB}$ vs F_{AB}. The logarithmic likelihood ratios are of course NF_{AB}, not F_{AB}, but we plot F_{AB} so that we can show that all points scatter about the dashed line, even though the number of events differs from energy to energy. For easy interpretation we label the scale as 10 000 δF_{AB} and 10 000 F_{AB}, corresponding to logarithmic likelihood ratios for typical 10 000-event samples. The points seem to scatter around the dashed line independently of

(i) the number of events (as just mentioned),

(ii) the number of parameters,

(iii) whether the events are real or Monte Carlo.

We have erected a vertical line at a ln-likelihood ratio of 3, and the standard test would say that to the right of this line solution B would begin to be ruled out. But consider the "X" plotted as far right as 4.5; its error 10 000 $\delta' F_{AB}$ is estimated to be 8.5, so that the value 4.5 is not an adequate reason for eliminating one hypothesis.

Our extra test agrees well with our studies (in Sec. V C) of actually casting out waves and refitting. Thus later in Table V we show the results of removing a wave (PP_{13}) whose amplitude $|T|$ appeared to be only 2 to 3 standards deviations from zero. After refitting, χ^2 went up only 11 (for Monte Carlo events) or 14 (for real events) but $\ln L$ decreased by 30 for both sets of events. We do not believe that the solution with the PP_{13} wave is e^{30} more likely than the solution without. But Fig. 8 shows that when $\Delta \ln L$ is 30, its error is about 10, and the significance test $F_{AB}/\delta' F_{AB} = \frac{30}{10} = 3$ seems quite reasonable.

In any case this extra test ($\delta' F_{AB} < F_{AB}$) offers a convenient numerical way to relate the result of several studies to the frequently occurring question: "Can we throw out this solution?" It is sufficiently conservative that we use it with considerable faith.

Finally we should point out the large *circles* plotted higher on Fig. 8. They are *not* $\delta' F_{AB}$, but just $\delta' F_A$ or $\delta' F_B$. These fluctuations in the ln-likelihood are of course much larger than the fluctuations in its ratio, but it is reassuring to note that as hypotheses A and B become significantly different, $\delta' F$ approach $\delta' F_{AB}$. We plot these δF dots for two reasons:

(i) We know that some older programs have used $\delta' F$ rather than $\delta' F_{AB}$ to compare competing solutions, and we want to warn that δF is too coarse.[28]

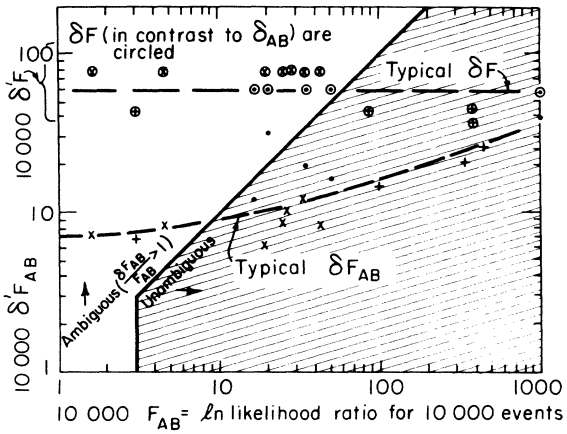

FIG. 8. Scatter plot of $\delta' F_{AB}$ vs F_{AB} used when trying to reject one of two competing local maxima A or B. F_{AB} is the average logarithmic likelihood ratio; $\delta' F_{AB}$ is its error. More precisely, $F_{AB} = (1/N)\ln[L(A)/L(B)]$, and $\delta' F_{AB}$ is calculated using Eq. (4.25). *Key to Symbols:* +: competing 18-wave fits to the 9000 Monte Carlo events of Table V; ×: 60-wave fits to 21 000 real events at 1890 MeV; dots: 20-wave fits to 10 700 events at 1690 MeV. For comparison, we have also plotted, as symbols with circles, the errors in the ln likelihoods themselves, δF.

(ii) Sometimes one knows that the two competing solutions are really very different, and it is of course easier to calculate $\delta' F$ rather than $\delta' F_{AB}$ since a program does not need to know about both hypotheses at the same time. In this case it is convenient to know that $\delta' F$ is an upper limit to $\delta' F_{AB}$.

G. Program tests

We made several checks on our programs:

(1) To ensure that we were calculating $X^c_{\alpha\mu}$ correctly in Eq. (3.2), we obtained the programs from three other analyses.[7,9,10] In all cases we got agreement[29] among the different programs.

(2) To test the fitting program itself, we generated artificial data from eleven "known" amplitudes and then fitted for the amplitudes. We generated 7583 events (4733 $N\pi^+\pi^-$ and 2850 $p\pi^-\pi^0$) at $\sqrt{s} = 1690$ MeV. To obtain a set of reasonable starting values, we generated 2000 sets of random amplitudes and kept the 20 sets with the highest likelihood. These 20 sets coalesced to five distinct solutions after fitting. Any wave among the 60 for which the modulus was within one standard deviation of zero in at least three solutions was considered statistically insignificant and eliminated. After elimination, we refitted with fewer waves and again eliminated waves. This was repeated a total of four times until no further waves

could be removed. All five solutions coalesced into one solution and the number of waves dropped from 60 to 24. These 24 waves consisted of the original 11 waves and another 13 waves, each of which had $|T|<0.05$. Figure 9 shows the initial 11 waves (as dots) and the corresponding 11 fitted amplitudes. The agreement is very reassuring, and gives us confidence that we can select the important waves for an original 60-wave hypothesis. However, in the case of real data, we are concerned with the extra uncertainties of fitting with an imperfect model, so we prefer to quote a "sensitivity" of $T=0.1$.

We also tried to break up the 7583 events into smaller samples of the order of 1000 events, but we found we needed all the events generated to get a good 60-wave fit. From this we decided to work with at least 10 000 events at each energy in order to make fits to 60 waves.

This completes our discussion of program tests made before we started fitting real events. More tests of realistic amplitudes (from fitting real events) are described in Sec. V C.

H. Limits for the observation of partial waves

From the tests above, and from our experience to be described in Sec. V, we estimate that there is sensitivity to any inelastic partial wave for which

$$T_\alpha > 0.1, \tag{4.26}$$

or, in terms of branching fractions $X_\alpha = \Gamma_\alpha/\Gamma$,

$$T_\alpha = (X_{el}X_\alpha)^{1/2} > 0.1 .$$

V. FITTING PROCEDURES, TESTS, AND QUALITY OF THE FINAL SOLUTIONS

A. Obtaining the 1972 24-wave solution "A"

The number and distribution of the events used in the analysis are given in Table III. The continuous distribution of events was binned into c.m. energy intervals of 30 or 40 MeV, except between 1560 and 1630 MeV, where no data were available. In this section we give an outline of the procedure used in obtaining our final solution. This procedure involved several distinct stages. The data were fitted in three parts: below 1560 MeV, 1630–1830 MeV, and above 1830 MeV.

(i) 1310–1560 MeV. In this region (9 bins) we reduced our 60 waves to 36 by removing all waves with $J \geq \frac{5}{2}$. In each of the six bins between 1380 and 1560 MeV, we generated 2000 random sets of amplitudes to use as starting values to the fitting program and kept the top ten. Any wave within two standard deviations of zero was considered statistically insignificant and removed. In this manner we were able, at each energy, to reduce to one solution. To look for continuity in energy we used each solution as a starting value for the neighboring energy bins. This new starting value always converged to the existing solution at that energy. Moreover, our $\vec{A}(E)$ varied smoothly with energy, providing a continuous solution. Below 1380 MeV, there were too few events for the fitting program to be able to distinguish between different solutions. In this region we propagated the solution from the bin above, removing all unnecessary waves.

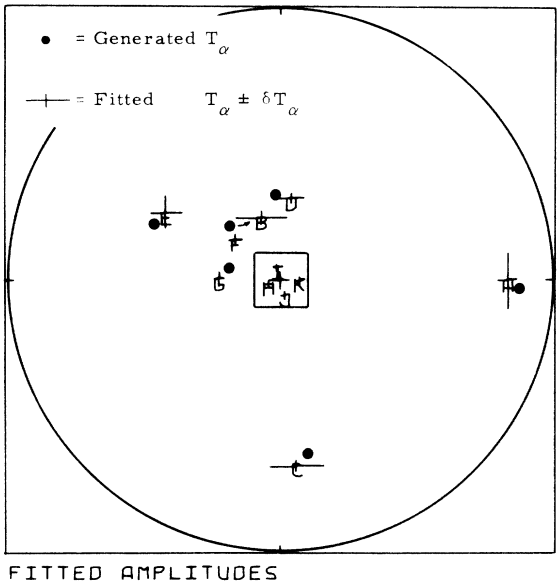

FIG. 9. Results of a fit to 7583 Monte Carlo events generated at 1690 MeV to test TRIANGLE/RUMBLE. The small square covers the area where we indeed reconstructed the four smallest waves, but also 13 "noise" waves. So we are insensitive to the area inside the square.

(ii) 1630–1830 MeV. In each of these five energy bins, we again generated 2000 random sets of amplitudes and this time kept the 20 with the highest likelihoods. From these twenty sets, we made fits with as many sets (10–15) as necessary to generate five distinct 60-wave solutions. We then made a list of all waves whose modulus was within 2.0 standard deviations of zero in three of the five solutions. These waves were removed and the solutions were refitted. This continued until no further waves could be removed. At this point, the five original solutions at each energy had reduced to two or three at that energy. However, the removed waves were different at each energy. We then returned to the 60-wave solution and removed all those waves which had been eliminated in at least three energy bins. Then we remaximized. We continued to remove waves that were unnecessary in at least three bins. In this

TABLE III. Number of events for the energy bins used in the fits. For availability of these events, see note at bottom of Table I.

c.m. energy	Range (MeV)	$\pi^- p \to \pi^+\pi^- n$	$\pi^- p \to \pi^-\pi^0 p$	$\pi^+ p \to \pi^+\pi^0 p$
i 1310	1300–1330	1069	151	
1340	1330–1360	1664	11	
1370	1360–1380	2471	2	
1400	1380–1410	5049	964	78
1440	1430–1460	4918	1802	359
1470	1460–1480	3252	1629	175
1490	1480–1510	5555	3197	1523
1520	1510–1530	3241	2588	795
1540	1530–1560	3905	3285	1114
ii 1650	1630–1670	6061	3757	2467
1690	1670–1710	5901	3689	1139
1730	1710–1750	3455	2630	4061
1770	1750–1790	3214	2352	2853
1810	1790–1830	2447	1541	3855
iii 1850	1830–1870	3931	3183	6372
1890	1870–1910	5072	3170	12 690
1930	1910–1950	5817	4080	4298
1970	1950–1990	5277	3544	7744
Total	1300–1990	72 299	41 575	49 523

way we reduced from 60 to 30 waves, but still had several competing solutions at each energy.

(iii) 1830–1990 MeV. Instead of using the full 60 waves, we started with the 30 waves from the lower energies together with the eight F_{35} and F_{37} waves which had been removed at lower energy. We generated 2000 random starts in this 38-wave set and kept only enough of the highest sets to give four separate solutions after fitting. Where possible, we again removed the unnecessary waves.

(iv) Continuity in energy above 1630 MeV. To look for continuity, we now used each solution as a starting value in the energy bin above and below its own. In more than half the cases, these starting values led to already existing solutions. If a new solution had a comparable likelihood ($\Delta F/\delta\Delta F < 1$), we not only kept it, but also used it as a starting value above and below its energy; and of course we checked that waves needed at $\sqrt{s} = 1540$ were present above the energy gap. In looking for smooth energy behavior, we found that some waves had discontinuous (almost random) behavior. We removed these waves even though the fitting program felt they were necessary. In 1972 we found only one chain of solutions over the entire energy range 1620–1999 MeV. This chain consisted of 20 waves from 1620 to 1710 MeV, 23 waves from 1710 to 1750 MeV, and 24 waves from 1750 to 1990 MeV. Figure 10 gives the waves needed at each energy. This is the point at which our analysis stood at the end of 1972 and this solution will be referred to as solution A.

B. The 1973 28-wave solution B

As we will discuss in Sec. VIC, the 1972 solution had some "undesirable" theoretical proper-

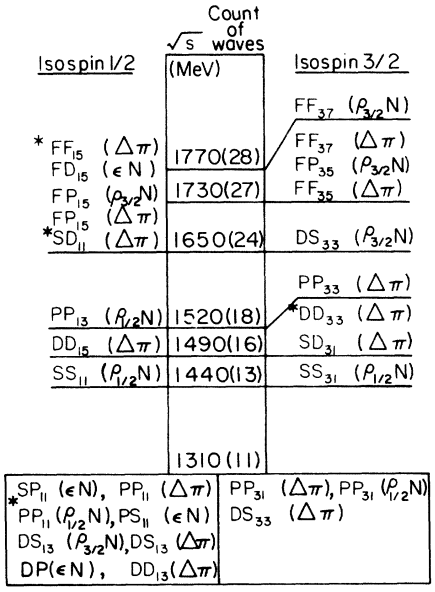

FIG. 10. Waves used in 1973 Solution B. In Solution A waves not used are indicated with an asterisk and D_{15} started later (at $\sqrt{s} = 1650$ MeV).

ties. In an effort to see if this solution was completely stable to the inclusion of new partial waves, we added some further amplitudes[30] to our 1972 set (those marked with an asterisk in Fig. 10), and repeated the fitting process. We found a new continuous solution in each energy range which differed dramatically from our previous solution only in the P_{11} waves and the new waves. However, as we shall see this has allowed us a further degree of flexibility in relating the partial-wave amplitudes in our two regions of analysis. In this case the final set contained 28 waves, and we will refer to this as solution B.

C. Tests and quality of our fits

1. *Four-dimensional* χ^2

To compare our fits with the data, we consider four-dimensional (or less) binning of our data. A *theoretical* bin population can be calculated by binning Monte Carlo events weighted by $p(\omega_i, \vec{A})$. The solid lines in Fig. 11 were generated for solution A in this manner. From these theoretical bin populations we can also calculate various χ^2 for the fit. Results are given in Table IV; 24 Dalitz plots corresponding to Fig. 11 are given in Ref. 20.

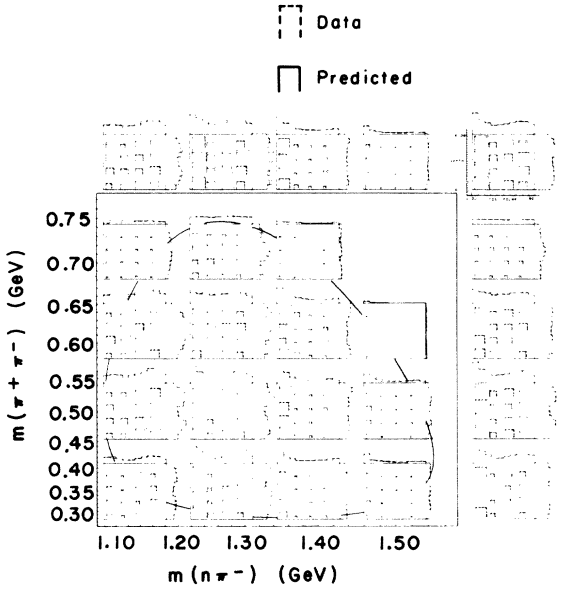

FIG. 11. Solution A fits to the reaction $\pi^- p \to \pi^+ \pi^- n$ at a c.m. energy of 1690 MeV. The figure contains $\cos\theta$ vs ϕ plots for individual regions of the Dalitz plot where $\cos\theta$ and ϕ are the angles of the incident pion in a coordinate system defined by the final state. The z axis lies along $\vec{p}_n$ and the y axis lies along $\vec{p}_{\pi^-} \times \vec{p}_{\pi^+}$. The plots outside the Dalitz plot are the sums of the corresponding plots within the boundary.

The purpose of using the maximum-likelihood technique is to take advantage of the many correlations that exist in the data, and thus the real test of our solutions lies in the ability to account for such correlations. As can be seen from Fig. 11 and the χ^2 values, we observe excellent reproduction of those correlations. This constitutes a major justification for our solutions.

2. *Agreement with total and partial-wave inelastic cross sections*

In Fig. 12 we demonstrate that the single-pion production cross sections[31] in the channels we fit are well reproduced. However, we can compare our prediction for

$$\pi^- p \to n\pi^0\pi^0 ,$$

$$\pi^+ p \to n\pi^+\pi^+ ,$$

which are not included in our analysis. This is done in Fig. 13, where we observe excellent agreement for $\sigma(n\pi^0\pi^0)$ but a large discrepancy for $\sigma(n\pi^+\pi^+)$. This latter fact may well have a simple physical interpretation and we return to this point in Sec. VII.

We can make even more stringent tests by comparing our inelastic partial-wave cross sections with the predictions from EPSA. At the lower energies where single-pion production is the major inelastic channel we find excellent agreement as demonstrated in the next section. However, at high energies, other inelastic channels begin to appear and the prediction from EPSA only becomes an upper bound on the single-pion production cross section, and this bound is satisfied at all energies.

3. *Removing waves, Monte Carlo checks*

At 1530 MeV we tested the final fit to see if our model was adequately describing the data. From the final amplitudes (R for "Real") we generated

TABLE IV. χ^2 at each energy based on four-dimensional bins. The four-dimensional space is subdivided into $4^4 = 256$ bins, but some have no population, hence the number tabulated below is < 250.

$\sqrt{s}$ (MeV)	$\chi^2_{n\pi^+\pi^-}$	Bins	$\chi^2_{p\pi^-\pi^0}$	Bins	$\chi^2_{p\pi^+\pi^0}$	Bins
1370	279	228				
1440	243	235	216	233	90	160
1530	328	229	253	236	209	216
1690	526	237	378	236	182	208
1970	864	236	601	233	907	235

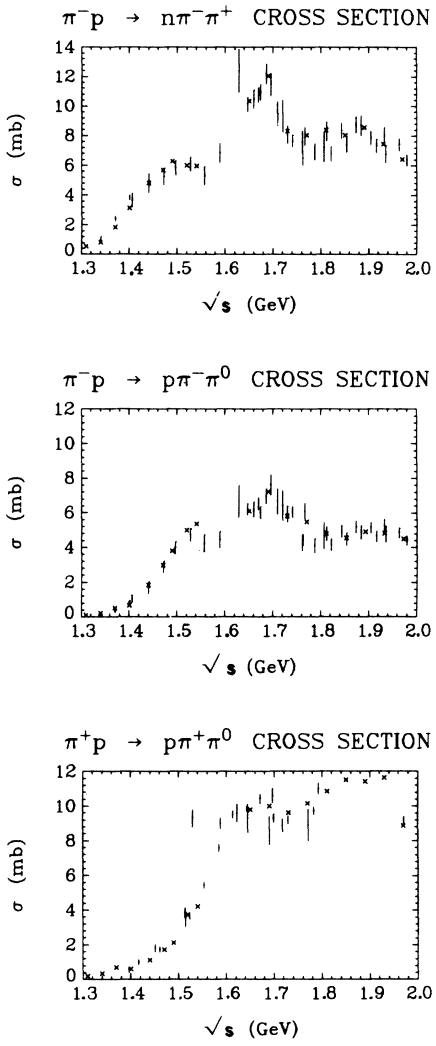

FIG. 12. Solution B cross sections for the fitted channels $n\pi^-\pi^+$, $p\pi^-\pi^0$, and $p\pi^+\pi^0$. Crosses correspond to our fits; tiny dots with vertical error bars are experimental, from Ref. 31.

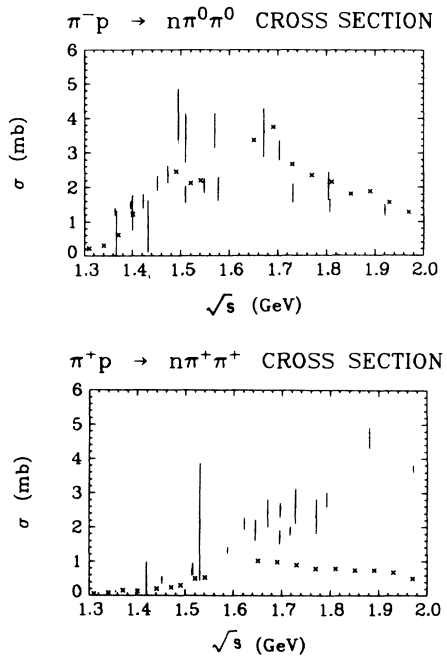

FIG. 13. Solution B cross sections predicted for the channels $n\pi^0\pi^0$ and $n\pi^+\pi^+$. Crosses are predicted from our fits to the other channels of Fig. 12; dots with vertical bars are from Ref. 31.

an equivalent number of Monte Carlo events. By fitting these Monte Carlo events, we determined a set of amplitudes T_{MC} which gave the best fit (within the errors we indeed found $T_{MC} = T_R$). From both fits T_R and T_{MC} we then removed a wave, refitted, and compared the changes in the likelihoods and in χ^2. The χ^2 was calculated by binning each variable into four bins ($4^4 = 256$ bins total). We did this for the four waves shown in Table V. The top wave listed, $DS_{13}(\rho_3 N)$ is a "large" wave having $|T|/\delta|T| \approx 10$ and its removal caused the other fitted T_α to move by many

TABLE V. Effect of removing waves of varying importance at $\sqrt{s} = 1530$ MeV, 9000 events. Each entry in the second and third columns in the lower part of the table is arranged $\Delta\, lnL$ for real events [$\Delta \ln L$ for Monte Carlo], and the same format holds for $\Delta\chi^2$.

		$\ln L$	χ^2/D.F.
Original 18-wave fit	Real	0.2817	790/681
	Monte Carlo	0.3198	624/788
	$\lvert T\rvert/\delta T$	$\Delta \ln L$	$\Delta\chi^2$
18 waves minus $DS_{13}(\rho_3 N)$	11 [10]	−320 [−390]	173 [215]
18 waves minus $PP_{33}(\Delta\pi)$	6 [6]	−60 [−80]	53 [102]
18 waves minus $PP_{13}(\rho_1 N)$	2 [3]	−30 [−30]	11 [14]
18 waves minus $DS_{33}(\rho_3\pi)$	1 [$\frac{1}{2}$]	−1 [−1]	3 [2]

standard deviations. The $PP_{33}(\Delta\pi)$ and $PP_{13}(\rho_1 N)$ are medium waves with $|T|/\delta|T| \approx 6$ and 3, respectively. The $DS_{33}(\rho_3 N)$ is a "small" wave with $|T|/\delta|T| \approx \frac{1}{2}$. Table V shows the results of these changes, which seem reasonable, and suggests that our program behaves properly. Since the results are the same for both the real and Monte Carlo events we believe our model fits the data adequately.

We also removed waves at higher energies: the $DD_{15}(\Delta\pi)$ wave at 1650 and the $FP_{15}(\Delta\pi)$ wave at 1690. The $DD_{15}(\Delta\pi)$ is the only D_{15} at 1650 and is quite large. Indeed $\ln L$ dropped by 584 when it was removed. The $FP_{15}(\Delta\pi)$ wave, however, is one of three F_{15} waves at 1690 and is only "medium" in size. Here $\Delta \ln L$ was 186. So again the program seems adequately sensitive to "medium" waves.

4. *Checks with a 60×60 error matrix*

After finding a best fit at each energy, we found it useful to calculate the full 60×60 error matrix, even though a satisfactory fit had been obtained with only, say, 20 waves. The idea behind inspection of the full error matrix is as follows: Suppose some untried wave, e.g. No. 59, is highly correlated with a wave used in the fit, e.g. No. 19. Then we had better try No. 59: We will probably find a new maximum with No. 59 as large as No. 19, and with No. 19 considerably changed. The clue that *some* wave is highly correlated with No. 19 can already be found in the diagonal elements of the error matrices, i.e., by comparing the error in 19 as computed in the 60×60 error matrix and in the 20×20 matrix. If the 60×60 error is, say, twice as big as the 20×20 one, we should look among the off-diagonal elements for large correlation coefficients such as $\langle \delta x \delta y \rangle_{19,59}$, where x and y can each be either amplitude or phase. A geometrical interpretation of the relation between the off-diagonal correlation and the increase in the diagonal error can be found in Fig. A1 of Appendix 1 of Ref. 20.

A 60×60 error matrix is too large to reproduce here (it is available in a supplement[44]); however, the diagonal elements only, for both 20×20 and 60×60 matrices, are compared in Table VI. We

TABLE VI. Square roots of diagonal elements of a 60×60 and a 20×20 (Solution A) error matrix at 1690 MeV.

$\Delta\pi$ wave	Error 20	Error 60	$\rho_3 N$ wave	Error 20	Error 60	$\rho_1 N$ wave	Error 20	Error 60	ϵN wave	Error 20	Error 60
ΔSD_{11}	···	0.083	$\rho_3 SD_{11}$	···	0.079	$\rho_1 SS_{11}$	0.054	0.069	ϵSP_{11}	0.066	0.087
ΔPP_{11}	0.061	0.076	$\rho_3 PP_{11}$	···	0.077	$\rho_1 PP_{11}$	···	0.080	ϵPS_{11}	0.067	0.084
ΔPP_{13}	···	0.083	$\rho_3 PP_{13}$	···	0.056	$\rho_1 PP_{13}$	0.038	0.053	ϵPD_{13}	···	0.064
ΔPF_{13}	···	0.053	$\rho_3 PF_{13}$	···	0.048	$\rho_1 DD_{13}$	···	0.057	ϵDP_{13}	0.042	0.054
ΔDS_{13}	0.045	0.063	$\rho_3 DS_{13}$	0.040	0.053	$\rho_1 DD_{15}$	···	0.041	ϵDF_{15}	···	0.047
ΔDD_{13}	0.044	0.058	$\rho_3 DD_{13}$	···	0.056	$\rho_1 FF_{15}$	···	0.040	ϵFD_{15}	0.027	0.032
ΔDD_{15}	0.052	0.068	$\rho_3 DD_{15}$	···	0.050	$\rho_1 FF_{17}$	···	0.033			
ΔFP_{15}	0.042	0.054	$\rho_3 FP_{15}$	0.033	0.042	$\rho_1 SS_{31}$	0.067	0.081			
ΔFF_{15}	···	0.052	$\rho_3 FF_{15}$	···	0.043	$\rho_1 PP_{31}$	···	0.090			
ΔFF_{17}	···	0.052	$\rho_3 FF_{17}$	···	0.041	$\rho_1 PP_{33}$	···	0.060			
ΔSD_{31}	0.062	0.075	$\rho_{35} D_{31}$	···	0.075	$\rho_1 DD_{33}$	···	0.057			
ΔPP_{31}	0.063	0.086	$\rho_3 PP_{31}$	···	0.083	$\rho_1 DD_{35}$	···	0.045			
ΔPP_{33}	0.062	0.096	$\rho_3 PP_{33}$	···	0.069	$\rho_1 FF_{35}$	···	0.040			
ΔPF_{33}	···	0.052	$\rho_3 PF_{33}$	···	0.047	$\rho_1 FF_{37}$	···	0.038			
ΔDS_{33}	0.049	0.075	$\rho_3 DS_{33}$	0.042	0.057						
ΔDD_{33}	···	0.052	$\rho_3 DD_{33}$	···	0.060						
ΔDD_{35}	···	0.065	$\rho_3 DD_{35}$	···	0.053						
ΔFP_{35}	···	0.048	$\rho_3 FP_{35}$	···	0.041						
ΔFF_{35}	···	0.050	$\rho_3 FF_{35}$	···	0.046						
ΔFF_{37}	···	0.053	$\rho_3 FF_{37}$	···	0.046						

see that the 60×60 errors are only 30% larger than their 20×20 counterparts, reassuring us that no highly correlated waves have been omitted.

Another use for the 60×60 error matrix is in making the transformation from partial-wave amplitudes, e.g. $\rho_1 N(FF_{15})$, $\rho_3 N(FP_{15})$, to helicity amplitudes, i.e., $\rho N(F_{15})$, $\lambda = \frac{1}{2}$, and $\frac{3}{2}$. One or two of the ρN partial waves may not have been needed in the fit, but clearly in making the transformation, the errors in these untried waves must be propagated along with the errors in the waves actually used.

D. Comparison of solutions A and B

In the above sections we have discussed the origin of solutions A and B and demonstrated that either corresponds to a good representation of the data available to date. We now make a quantitative comparison of the two solutions.

In Table VII a summary of the differences in likelihoods of solutions A and B is given at nine energies between (1640–2000) MeV (evaluated for a standard sample of 9000 events). For each energy, solution B gives the higher likelihood, and the difference is around 100. Since solution B involves four additional partial waves compared to solution A, we must determine whether this increase of 25 per wave in the likelihood function is significant. Reference to Table V, where we discuss the sensitivity of our solutions to the removal of waves, indicates that such a change in likelihood corresponds to that expected for the inclusion of three or four waves with $|T|/\delta T \sim 3.0$ (i.e., quite significant, moderately large waves). Thus we conclude that the four new waves are really required and that solution B provides a substantially better representation of the data than the original solution A.

E. Summary

We find two solutions which possess all the following properties:

(i) At each energy the solution parameters correspond to a maximum in the likelihood function and have a high likelihood (usually the highest of the competing solutions).

(ii) The solution at each energy propagates to the solution at the adjacent energies above and below.

(iii) Qualitatively it has no discontinuous motion between adjacent energies.

(iv) It possesses good agreement with the EPSA predictions for the inelastic cross sections.

The crucial step was the selection of a good subset of waves. Our two final subsets were the only ones we found that had solutions satisfying all the above requirements. Owing to cost of computer time we cannot be certain that we have found the only two subsets. But we believe that the larger waves are uniquely determined. We cannot be as certain in the case of the smaller waves, the amplitudes of which are never more than two or three standard deviations from zero. Furthermore, with 30–40 MeV energy bins, our emphasis on continuity clearly biases us against very narrow resonances.

TABLE VII. Difference in likelihood, L (Solution B)–L (Solution A) for a standard sample of 9000 events. Solution B is always better.

$\sqrt{s}$ (MeV)	$\Delta \ln L$ (9000 events)
1650	113
1690	122
1730	139
1770	107
1810	84
1850	57
1890	15
1930	153
1970	19

VI. THE PARTIAL-WAVE AMPLITUDES–DESCRIPTION AND DISCUSSION

At each energy the solutions of any fits to inelastic data are only defined up to an overall phase. Thus, in order to give Argand diagrams of the partial-wave amplitudes we must determine this phase. Of the variety of methods by which this can be achieved, we have linked the inelastic amplitudes to published elastic amplitudes (which have known phase) via a K-matrix fit at energies where both elastic and inelastic amplitudes are large[32]—this turns out to be in the region of a prominent resonance. This has been done for both solutions A and B.

In Figs. 14 and 15 we present summary Argand diagrams for solutions A and B, and in Fig. 16 both Argand diagrams and partial-wave cross sections for solution B. The equivalent complete figures for solution A are contained in Ref. 11. A summary of the major characteristics of each partial wave is given in Table VIII, together with comments on resonance interpretations. For the specialist, numerical values for the amplitudes, and decks of cards, are available.[44]

Next we discuss the unambiguous results in our two solutions and contrast the differences between them. Before entering into too great detail we should note that the major difference between the

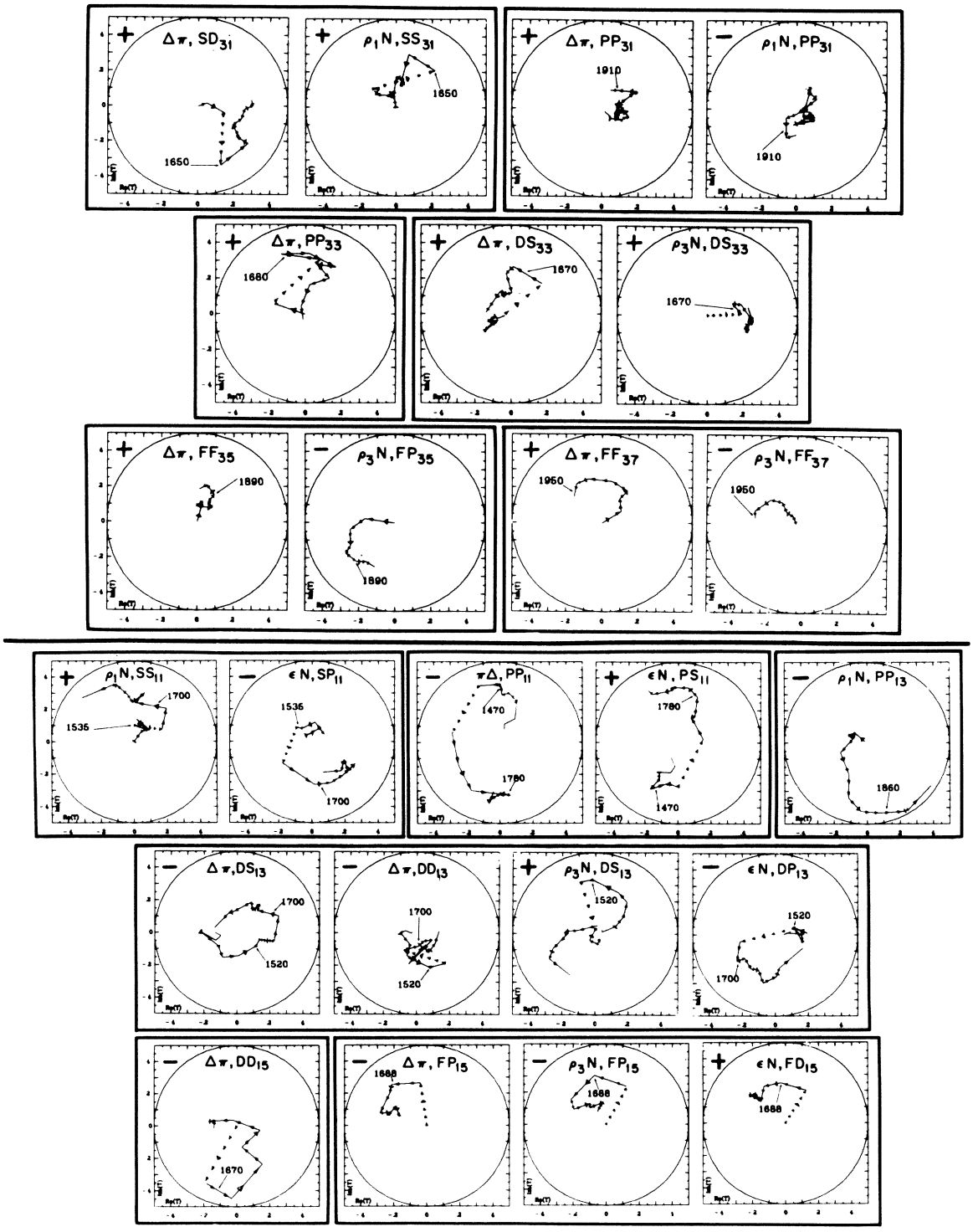

FIG. 14. Summary $N\pi\pi$ Argand plots for solution A (1972). Nominal resonance energies come from the CERN 1972 EPSA (Ref. 1). For more details see caption to Fig. 16.

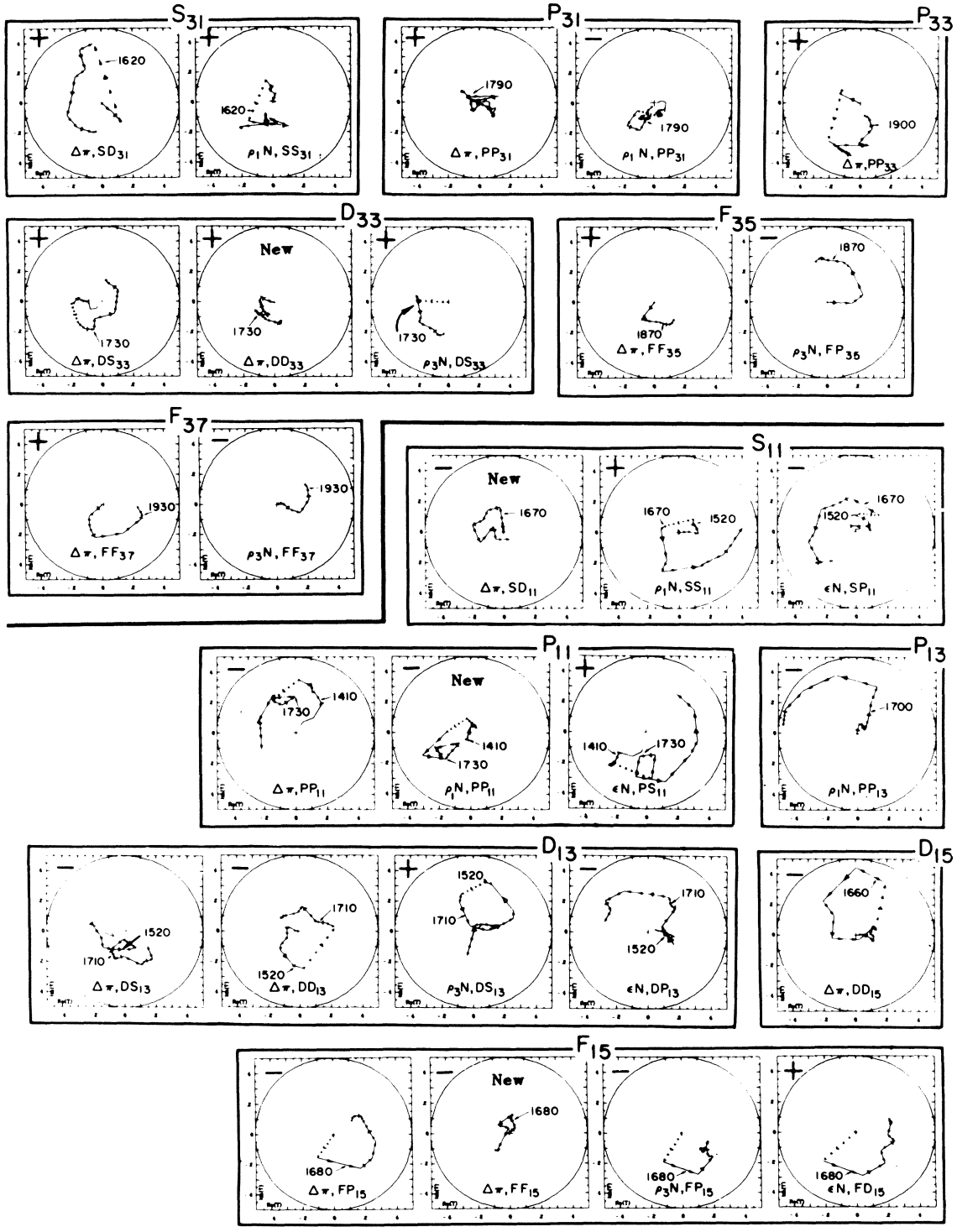

FIG. 15. Summary $N\pi\pi$ Argand plots for solution B (1973). Nominal resonance energies come from the Saclay 1973 EPSA (Ref. 2). For more details see caption to Fig. 16. Numerical values are available in the supplement.[44]

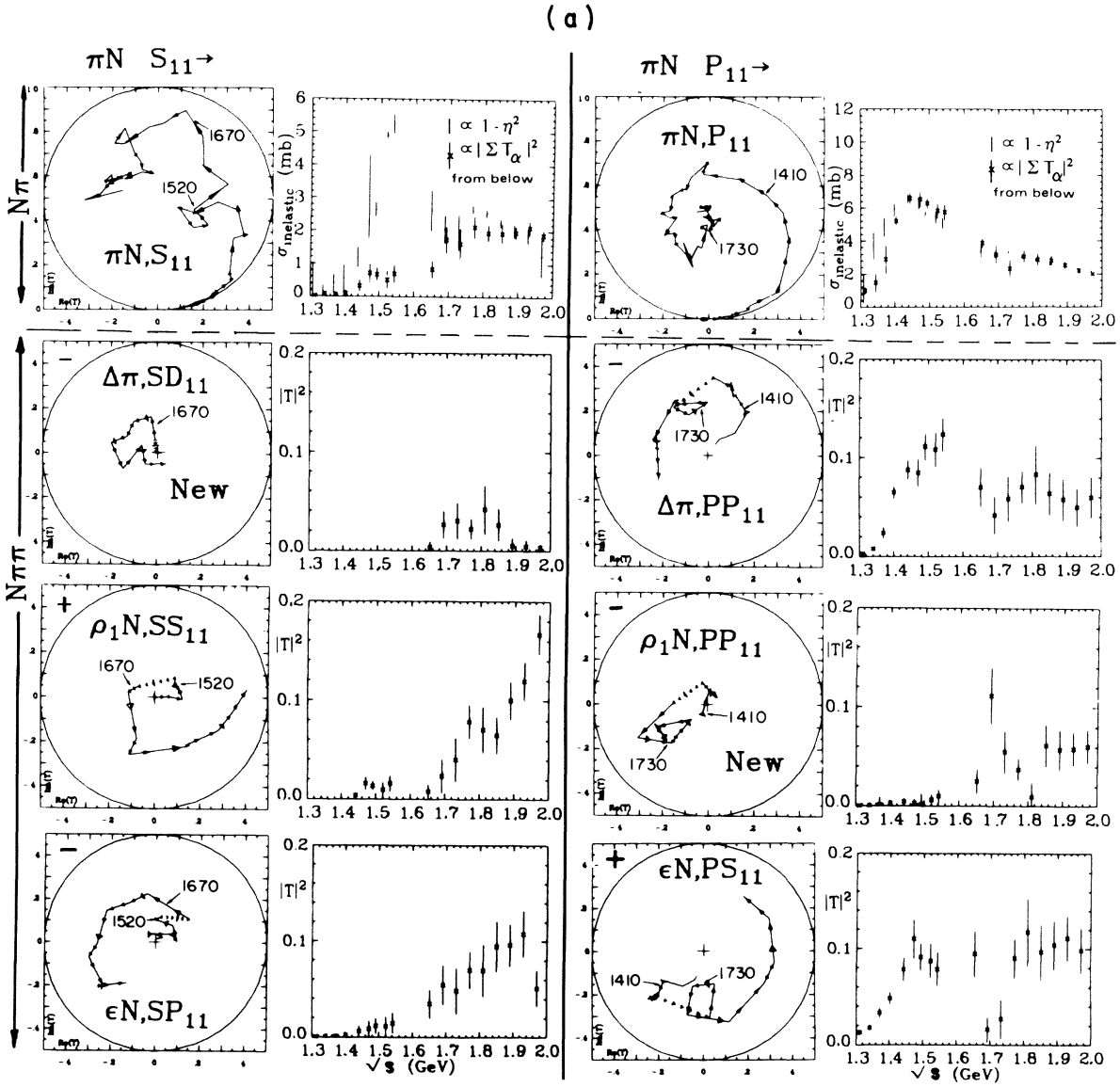

FIG. 16. *(Continued on following page)*

two solutions lies in the relative orientation of the low-energy (1300–1540 MeV) and high-energy (1630–2000 MeV) amplitudes. This flexibility is due solely to the fact that we have not been able to analyze data in the "gap," and clearly the correct solution will be identified when this is done reliably. It is important to point out that within each energy regime, solutions A and B are essentially identical, except in the P_{11} waves and the new waves added. All of the major features remain the same provided one does not try to link the two energy regions.

A. $I=\frac{1}{2}$ states

The considerable amount of motion in these plots is not surprising since most of the structure observed may be associated with the existence of already established resonant states.

1. P_{11}. In both solutions, the $P_{11}(1470)$ is clearly observed decaying strongly into $\pi\Delta$ and $N\epsilon$. A higher-mass P_{11} is also present in both solutions, although there are distinct differences in shape in this case.

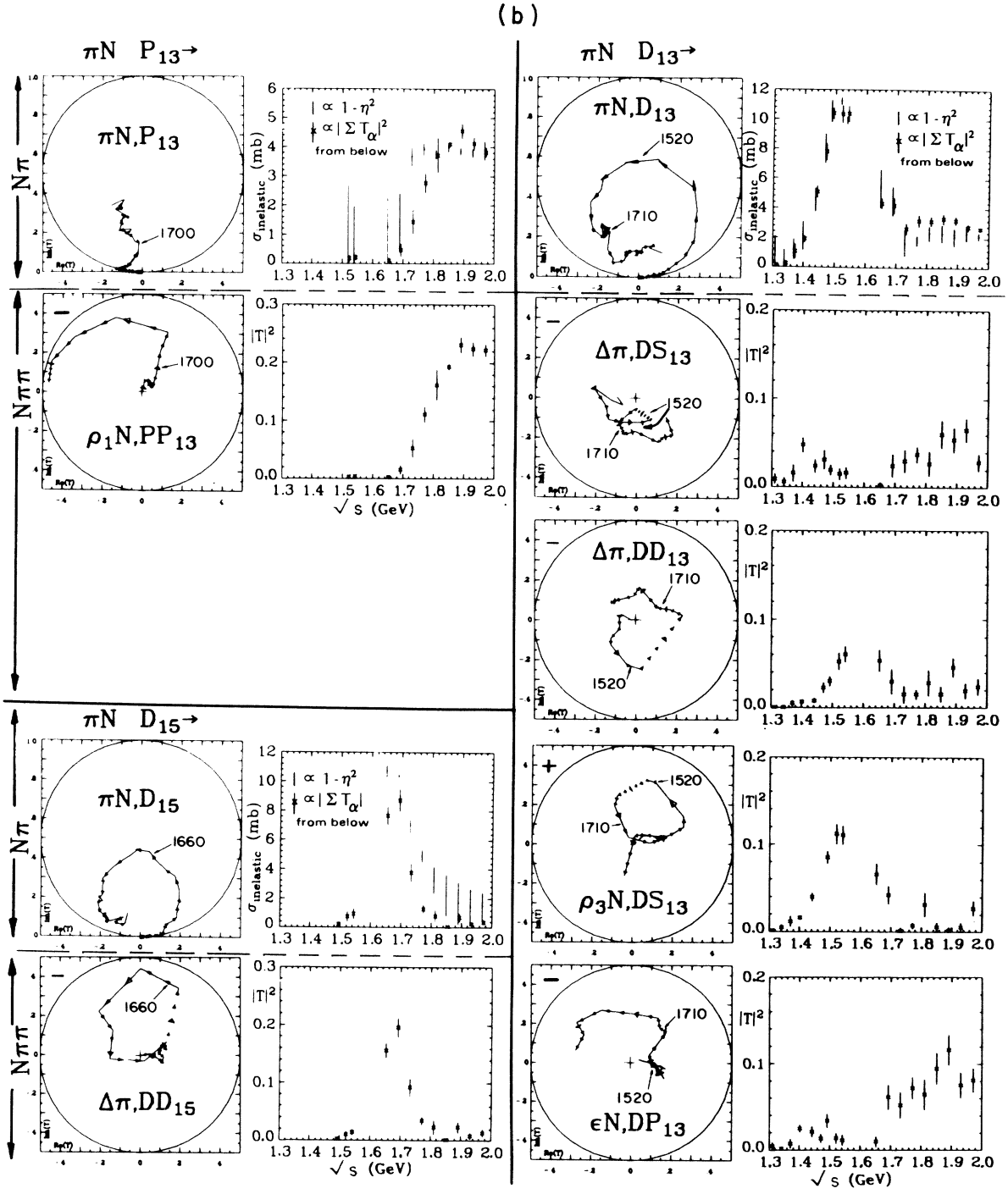

FIG. 16. *(Continued on following page)*

2. Nρ couplings. We observe strong $N\rho$ couplings of the $P_{13}(1700)$, $D_{13}(1520)$, and $F_{15}(1680)$ resonances. This is not surprising, as the last two resonances are strongly seen in photoproduction and application of the vector dominance model would imply this result. In the case of the new $P_{13}(1700)$, $N\rho$ is the major decay channel.

3. $D_{13}(1700)$. This state is observed in our solutions. Its presence is predicted[33] by the L excitation quark model and is the last remaining N^* or Δ state of the (70, 1^-) supermultiplet of negative-parity baryon states to be identified. It

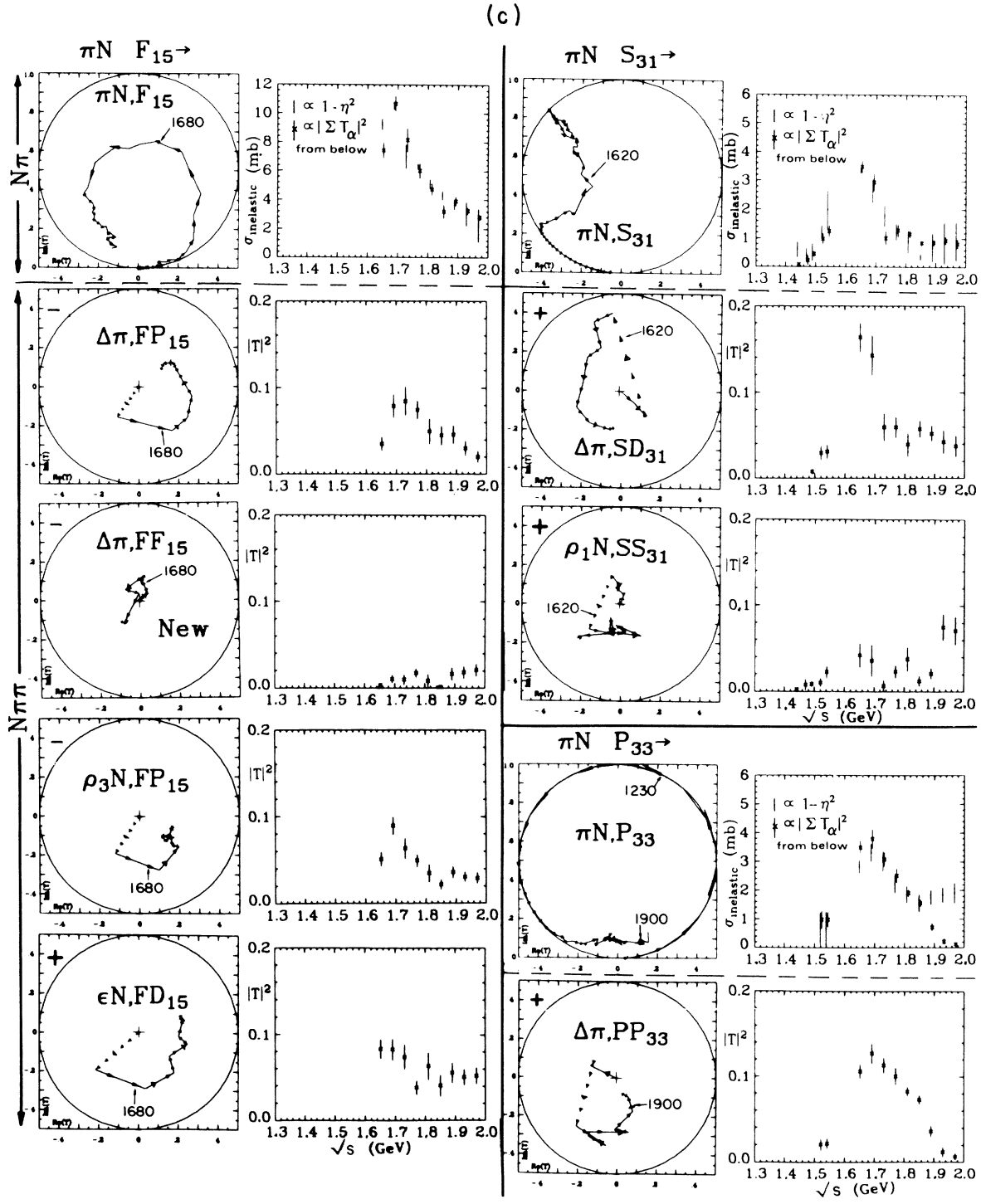

FIG. 16. *(Continued on following page)*

decays into the $\pi\Delta(DS_{13})$ and $N\epsilon(DP_{13})$ channels, but its mass and width are difficult to estimate and probably differ between our solutions A and B.

4. *D_{15} and F_{15}.* These two resonances are strongly observed in our analysis. This verifies our previous result that the D_{15} couples exclusively (within errors) to the πN and $\pi\Delta$ channels. Moreover, we have now determined unambiguously the relative sign of the F_{15} and D_{15} $\Delta\pi$ couplings and

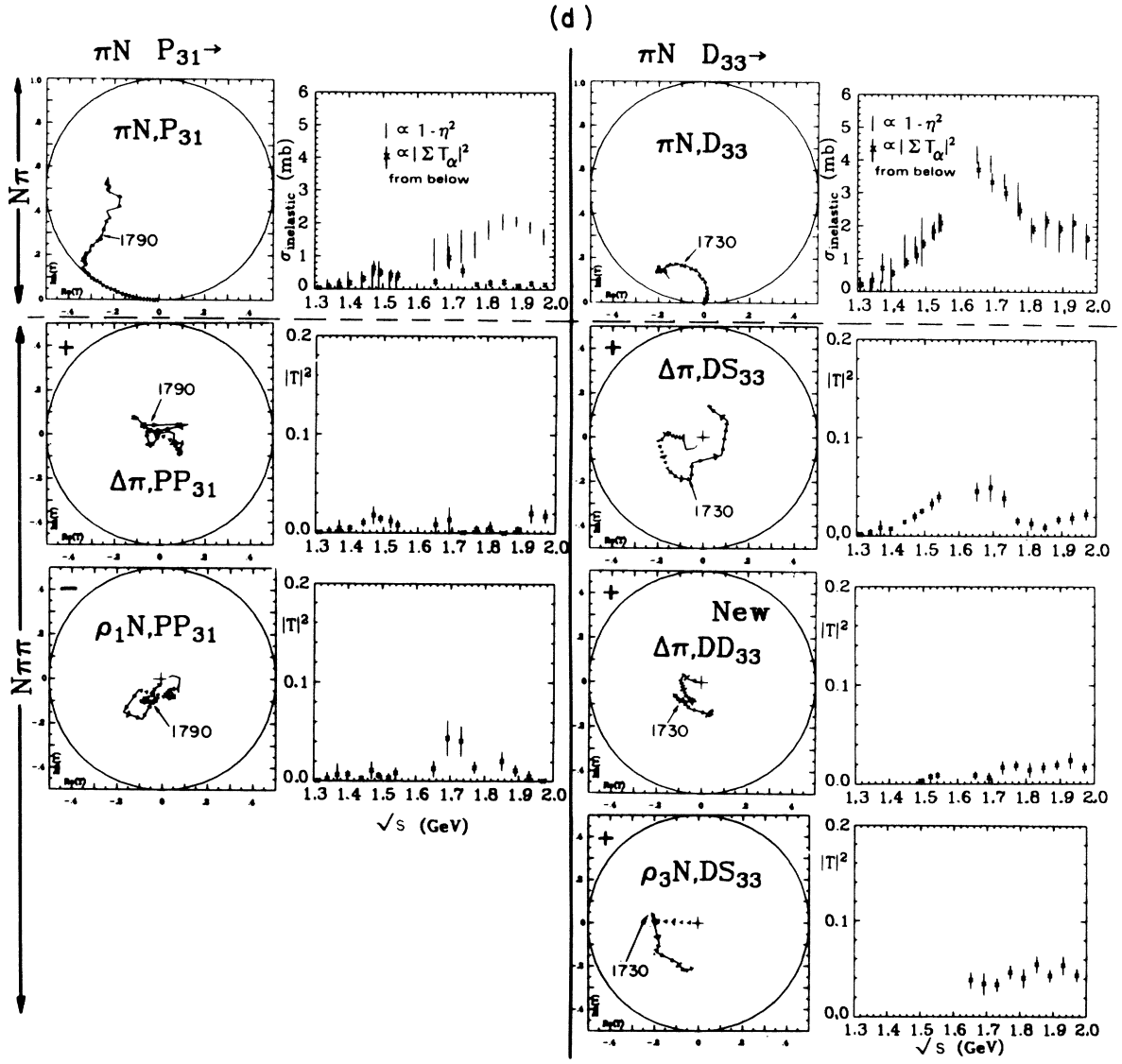

FIG. 16. *(Continued on following page)*

accounted for all the F_{15} inelasticity. Thus we have made a significant improvement over our previous analysis.[4]

5. *Nϵ decay modes.* In our analysis the ϵ is a slowly varying effect over the Dalitz plot. Hence $N\epsilon$ decays may also be interpreted as direct three-body $\pi\pi N$ decays of a given J^P.

B. $I=\frac{3}{2}$ states

1. For $E<1540$, all of the $I=\frac{3}{2}$ amplitudes are small, whereas for $E \geq 1650$ MeV (where we again have data) the S_{31}, D_{33}, and P_{33} amplitudes are already large. This means that we cannot observe the complete anticlockwise motion in these channels.

2. The presence of two low-energy P_{11} states (~1410 and ~1730 MeV) implies the need for two P_{33} states in most schemes, while the ($\underline{56}$, $L=2^+$) supermultiplet requires yet a third. In terms of partial-wave analyses, the situation is confused—the two EPSA's disagree; likewise our solutions A and B. We compare the CERN and Saclay parameters:

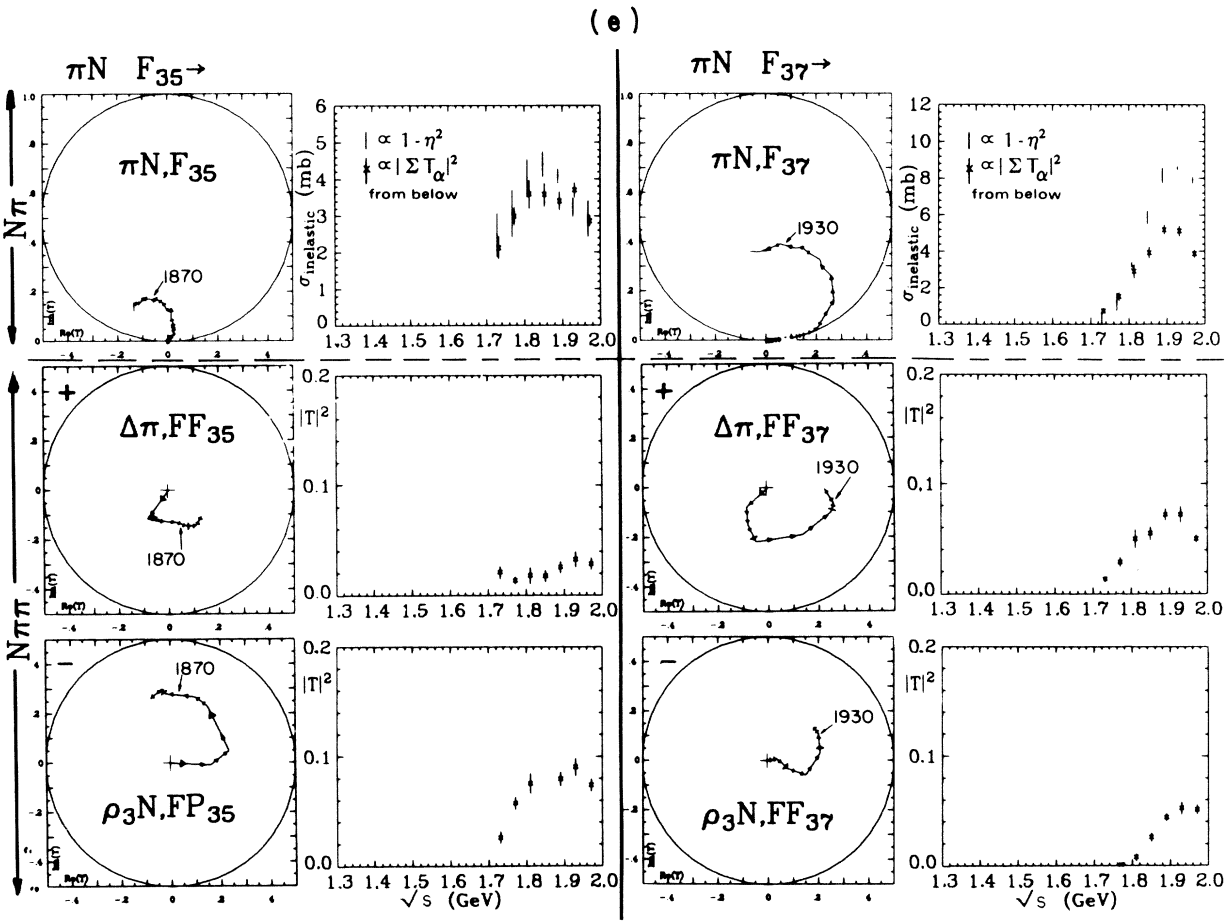

FIG. 16. (a)–(e) Argand diagrams and partial-wave cross sections for the elastic and inelastic channels. The elastic solutions are from CERN 1972 (Ref. 1). The inelastic channels are our 1973 solution B. On the Argand plots the nominal resonance energies come from Saclay 1973 (Ref. 2). Arrowheads are spaced every 20 MeV, with a wider arrowhead at integral hundreds of MeV. Lower-l waves are plotted starting at $\sqrt{s}=1400$ MeV; higher-l waves start where introduced into the fit. Last arrowhead is always at 1940 MeV. To show the gap in our data the straight line joining the five arrows in the gap has been deleted. The + or − signs at the upper left of each circle show how to transform from our sign conventions to the "baryon-first" convention. "New" indicates one of the four waves used in solution B only. Nine ρ_1 and ϵ signs were changed 5 July 1974. Facing each inelastic Argand diagram of T_α, we plot $|T_\alpha|^2$ vs $\sqrt{s}$. Facing the top (elastic) Argand plot, the total $\sigma_{\text{inelastic}}$ ($\propto 1-\eta^2$), derived from EPSA, is compared with the sum of the σ_{in} from each isobar-model channel plotted below. The small interference terms between channels are taken into account; see Eq. (3.7). Note that the σ's, as plotted, are labeled by isospin, not charge, so to get $\sigma(\pi^- p \to N\pi\pi)$ one must use $\frac{2}{3}\sigma(I=\frac{1}{2})+\frac{1}{3}\sigma(I=\frac{3}{2})$. Numerical values for our amplitudes are listed in Ref. 44.

	Mass (MeV)	Γ (MeV)	γ	Authors' own "crude" estimate of resonance quality
CERN[1]	1680	220	0.1	poor
Saclay[2]	1900	204	0.19	good, but in need of clarification

Our solution A does not show these resonances, but our preferred solution B is consistent with the existence of both.

3. F_{35}. In both solutions A and B we have evidence for an F-wave $\pi\Delta$ system, as do Mehtani *et al.*,[5] although one might expect, on kinematical barrier-factor arguments, the P wave would dominate. In our solution the decay into $N\rho$ domin-

TABLE VIII. Characteristics of each partial wave.

Partial wave	EPSA results (Ref. 2)	Discussion of our results	Decay channels and general comments on our results for Solution B
S_{11}	$M = 1520$; $\chi_{\text{inel}} \sim 0.45$	Not clearly observed in our data; this is consistent with a large branching fraction (~ 0.55) into ηN (see Ref. 3).	πN, ηN
	$M = 1670$; $\chi_{\text{inel}} \sim 0.85$	Resonant loops are clearly present in the ϵN and ρN channels. Some evidence of coupling to $\pi\Delta$.	πN, ϵN, ρN, $\pi\Delta$
	$M \sim 2280$; χ_{inel}	Not sensitive to this state above our energy range.	πN
P_{11}	$M \sim 1410$; $\chi_{\text{inel}} \sim 0.45$	Resonance behavior in $\pi\Delta$ and $N\epsilon$ channels.	πN, $\pi\Delta$, ϵN
	$M \sim 1730$; $\chi_{\text{inel}} \sim 0.85$	All channels show a small loop, distinctly narrower than EPSA width of 164 MeV.	πN, $\pi\Delta$, ϵN
P_{13}	$M = 1700$; $\chi_{\text{inel}} \sim 0.85$	Clear resonant behavior is observed in the ρN channel.	πN, ρn strengthens the observation in EPSA
D_{13}	$M \sim 1520$; $\chi_{\text{inel}} \sim 0.45$	Strong resonant behavior in the $N\rho$ and $\pi\Delta$ channels (even though $N\rho$ is 300 MeV below threshold).	πN, ρN, $\pi\Delta$
	$M \sim 1710$; $\chi_{\text{inel}} \sim 0.9$	Clear resonant motion in ϵN and $\pi\Delta$, but distinctly broader than EPSA width of 100 MeV.	πN, ϵN, $\pi\Delta$ First unambiguous observation of resonant behavior in this region
D_{15}	$M = 1660$; $\chi_{\text{inel}} \sim 0.6$	The $\pi\Delta$ channels show strong resonant behavior, saturating the unitary bound near the accepted resonant mass.	πN, $\pi\Delta$
F_{15}	$M = 1680$; $\chi_{\text{inel}} \sim 0.4$	This resonance is observed in ϵN, ρN, and $\pi\Delta$ with comparable strength.	πN, ϵN, ρN, $\pi\Delta$
S_{31}	$M = 1620$; $\chi_{\text{inel}} \sim 0.70$	We lack the experimental data which would reveal the behavior of this wave in the resonance region. The present points above 1650 show a smooth behavior which is compatible with the accepted resonance mass.	πN, $\pi\Delta$, ρN
P_{31}	$M = 1790$; $\chi_{\text{inel}} \sim 0.85$	No evidence for resonant behavior.	πN
P_{33}	Suggestion of resonance with $M \sim 1900$; $\chi_{\text{inel}} \sim 0.8$	Fast $\Delta\pi$ motion across gap suggests resonance near 1700, i. e., below EPSA value of 1900. [See discussion in Sec. VI. B2.]	πN, $\pi\Delta$
D_{33}	$M \sim 1720$; $\chi_{\text{inel}} \sim 0.85$	Our analysis is consistent with a resonance interpretation for $\pi\Delta$ and ρN.	πN, $\pi\Delta$, ρN
F_{35}	$M \sim 1870$; $\chi_{\text{inel}} \sim 0.85$	Strong resonance behavior seen in ρN channel smaller coupling to $\pi\Delta$.	πN, ρN, $\pi\Delta$
F_{37}	$M = 1930$; $\chi_{\text{inel}} \sim 0.6$	Clear resonance behavior is apparent in ρN and $\pi\Delta$ channels.	πN, ρN, $\pi\Delta$

ates, and this final state allows us to saturate the EPSA inelastic cross section prediction.

4. F_{37}. This resonance is observed both in the $\pi\Delta$ and $N\rho$ channels. However, these two channels do not saturate the predicted inelastic cross section (only ~60% is accounted for). The strong $N\rho$ decay might well be expected again as this resonance is a dominant feature of photoproduction.

5. P_{31}, D_{35}. These waves fall short of the EPSA predictions. In particular we find no need for any D_{35} interactions, i.e.,

$$\sigma_{\text{in}}(D_{35}) = 0 .$$

Thus, if there are any low-lying D_{35} resonances they do not couple to the $\pi\Delta$ or $N\rho$ channels. However, EPSA does predict a large inelastic cross section from the wave (~4 mb), and this is a shortcoming of our results, although it probably has a simple interpretation. [See E 1 below.]

C. The origin of solution B and the new waves added

We were motivated to study the stability of solution A by the observation that some of the relative coupling signs between resonances in our lower-energy region and resonances in our upper energy region (in solution A) conflicted with the predictions of broken $SU(6)_w$ (Ref. 30) and Melosh transformations,[34] although within each energy region there was consistency with theory. Thus we studied several ways in which another continuation of the partial-wave amplitudes across the energy gap might be achieved. A second solution—our solution B—was found in the following manner. We added many new waves (admittedly suggested by theory[30]) and reperformed our whole fitting process. This led to the new solutions in the two energy regions which allow a different continuation through the energy gap and hence the new solution B. This solution is an even better fit to the data than solution A, and furthermore the signs of the $DD_{13}(1520)$ and $DD_{15}(1660)$ are now in good agreement with the theoretical expectations.

The four new waves are SD_{11} in $\pi\Delta$, DD_{33} in $\pi\Delta$, FF_{15} in $\pi\Delta$, and PP_{11} in $N\rho_1$.

From the previous discussion of this section it is clear that within the energy regions in which we have data there is little difference between these solutions. The important test lies in the "gap" through which we have to make a K-matrix extrapolation. Thus this result emphasizes the need for the free availability of complete data sets or at least a reliable partial-wave analysis in the energy region 1540–1630 MeV.

D. Resonance parameters

We have resisted the temptation to quote any resonance parameters in this paper. The problem of extracting these quantities is difficult and is the subject of the companion papers.[32,35–38]

E. Further comments

We would like to call attention to some conclusions we may draw from the absence of certain waves (D_{35}), the failure to reach EPSA predictions (P_{31}, F_{37}), the poor fits to the $\pi^+\pi^+n$ state, and the general deterioration of the fits at the higher energies.

1. $\pi^+\pi^+n$ and $N^*_{1/2}$ final-state interactions

Our predictions for $\sigma(\pi^+\pi^+n)$ are a factor of 2 too small (~2–3 mb unaccounted) at the higher energies. This is not surprising, as only the $\pi\Delta$ intermediate states of our isobar model connect with this final state, and from inspection of the π^+n mass spectra it is clear that $N^*_{1/2}$ isobars ($P_{11}, D_{13}, F_{15}, D_{15}$) may be present. Furthermore, if one considers low angular momenta in the $\pi N^*_{1/2}$ system one finds

$$\left.\begin{array}{l}\pi N^*(D_{13}) \text{ in a } P \text{ wave} \\ \pi N^*(F_{15}) \text{ in an } S \text{ wave}\end{array}\right\} \text{ are derived from } D_{35} ,$$

$$\pi N^*(P_{11}) \text{ in an } S \text{ wave would be derived from } P_{31} ,$$

which suggests that our previously noted failure to reach the P_{31} and D_{35} predictions is associated with not including N^* final-state interactions. This suggestion can be further substantiated if we note that

$$\sigma_{\text{missing}}(P_{31} + D_{35} + F_{37}) \simeq \sigma_{\text{missing}}(\pi^+\pi^+n) + \sigma(\pi\pi\pi N) .$$

Finally, the inclusion of these waves would have an appreciable effect in the $\pi^+\pi^+n$ final state, whereas Clebsch-Gordan coefficients reduce their effect in the other single-pion production reactions so that our analysis of those channels would probably show little change.

2. Peripheral nucleon

The deterioration of the fits at higher energies is generally associated with being unable to entirely account for the onset of peripheral processes. This probably indicates the necessity for inclusion of π exchange in the production of the $N\rho$ final state, so that higher partial waves are generated.

VII. CONCLUSIONS

Elastic phase-shift analyses only relate to one aspect of the πN interaction, and the analysis described here represents a substantial progress in providing complementary information on the inelastic channels.

This analysis has demonstrated that isobar-model partial-wave analyses of inelastic final states can reproduce the detailed nature of the data. This then allows the observation of resonances in inelastic channels.

We have evidence for the existence of a $D_{13}(1700)$, long predicted by the quark model. The existence of a $P_{13}(1700)$ is corroborated through a strong ρN coupling. Our preferred solution B indicates a $P_{33}(1700)$ resonance. Furthermore, we have strengthened the interpretation of many resonances due to our observation of them in the inelastic channels $N\rho$, $N\epsilon$, and $\pi\Delta$.

Earlier analyses have produced limited $\pi\Delta$ Argand plots, but this analysis presents the first full Argand plots for all three channels, $N\rho$, $N\epsilon$, and $\pi\Delta$. These begin to allow a complete picture of the πN interaction, accounting for almost all of the inelastic cross section.

Finally, we are at present using these amplitudes to study resonance parameters and couplings and their relations in other theories of hadron interactions.[32,35-38]

ACKNOWLEDGMENTS

We wish to thank the Oxford, UCR-LBL, and Saclay groups, especially A. Jones, D. Saxon (Oxford), S-Y Fung, G. Kalmus, A. Kernan, W. Michael (UCR-LBL), B. Deler, Nguyen Thuc Diem, and J. Dolbeau (Saclay), for use of their data in this analysis. We also thank J. P. Berge, A. D. Brody, B. Deler, A. Kernan, B. Levi, L. R. Price, and B. Shen for their contributions to the early phase of the experiment. We further wish to thank D. Faiman, F. Gilman, and M. Kugler for their interest and suggestions.

APPENDIX A: MAXIMIZING THE SCALE PARAMETER IN THE LIKELIHOOD FIT

In Eq. (4.11) remember that $N^c R^c/\sigma^c$ is the number of events ν^c predicted by the parameters $\vec{A}$, so write

$$\sum \frac{N^c R^c}{\sigma^c} = \sum \nu^c(\vec{A}) \equiv \nu(\vec{A}) .$$

For this discussion the first product in Eq. (11) is only a constant B which does not depend on $\vec{A}$, so Eq. (4.11) becomes

$$L = Be^{-\nu(\vec{A})} \prod_{i=1}^{N} p_i(\vec{A}) . \tag{A1}$$

Introducing the scale factor of Eq. (4.12),

$$\vec{A} = s\vec{A}^0 , \tag{A2}$$

we have

$$\nu(s\vec{A}^0) = s^2 \nu(\vec{A}^0) \equiv s^2 \nu^0$$

and

$$\prod p_i(s\vec{A}^0) = s^{2N} \prod p_i(\vec{A}^0) .$$

Equation (A1) becomes

$$L(s\vec{A}^0) = Be^{-s^2\nu^0} s^{2N} \prod p_i(\vec{A}^0) , \tag{A3}$$

and the last factor $\prod p_i$ is independent of s. Combining it with B, we have

$$L(s\vec{A}^0) = B'e^{-s^2\nu^0} s^{2N} . \tag{A4}$$

Then

$$\ln L(s\vec{A}_0) = \ln B' - s^2\nu^0 + 2N \ln s$$

and

$$\frac{\partial}{\partial s} \ln L(s\vec{A}_0) = -2s\nu^0 + \frac{2N}{s} . \tag{A5}$$

To find $s^2|_{L\,\max} \equiv s_m^2$, set (A5) = 0, and we get Eq. (4.18), i.e.,

$$s_m^2 = \frac{N}{\nu_0} = \frac{N}{\sum N^c R^c(\vec{A}_0)/\sigma^c} . \tag{A6}$$

Equation (A6) is derived in Miller's thesis,[23] but there s^2 is written by mistake as s. We now insert our result (A6) into (A4),

$$L(s_m\vec{A}^0) = B'e^{-N}\left(\frac{N}{\nu_0}\right)^N , \tag{A4m}$$

and this in turn into (A3)

$$L(s_m\vec{A}^0) = Be^{-N}\left(\frac{N}{\nu^0(\vec{A}_0)}\right)^N \prod_{i=1}^{N} p_i(\vec{A}^0) . \tag{A3m}$$

Now that s is maximized, we see that (A3m) is independent of the over-all magnitude of $\vec{A}^0$, and we can drop its superscript zero and call it $\vec{A}$. For the purpose of searching in $\vec{A}$ space for $L_{\max}$ we emphasize factors containing $\vec{A}$:

$$L(s_m\vec{A}) = Be^{-N} N^N \left[\sum \frac{N^c R^c(\vec{A})}{\sigma^c}\right]^{-N} \prod_{i=1}^{N} p_i(\vec{A}) , \tag{A7}$$

$$\ln L(s_m\vec{A}) = \text{const} - N \ln\left[\sum \frac{N^c R^c(\vec{A})}{\sigma^c}\right] + \sum_{i=1}^{N} \ln p_i(\vec{A}) .$$

We actually work with the average of this premaximized L, which we call $F(\vec{A})$,

$$F(\vec{A}) = \frac{1}{N} \ln L(s_m \vec{A}), \tag{A8}$$

$$F(\vec{A}) = \text{const} - \ln\left[\sum_c \frac{N^c R^c(\vec{A})}{\sigma^c} \right] + \frac{1}{N} \sum_{i=1}^{N} \ln p_i(\vec{A}). \tag{A9}$$

The factor $1/N$ in (A8) makes F roughly independent of N, so it is easier to compare fits at different energies where there are different numbers of events. Equation (A9) is the same as Eq. (4.20) of the text.

APPENDIX B: EXAMPLE OF STEPPING PROCEDURE WHEN $\nabla\nabla^T f$ MATRIX IS SINGULAR

As an example of the method discussed in Section IV D 4, consider the function $f(z) = -z^2 + 2z + 1$, but let $z = x + y$, i.e.,

$$f(x, y) = -(x+y)^2 + 2(x+y) + 1, \tag{B1}$$

where f has a maximum at $z = x + y = +1$. In this case, we clearly have a redundant parameter. Now

$$\nabla f = 2[1 - (x+y)] \begin{pmatrix} 1 \\ 1 \end{pmatrix} \tag{B2}$$

and

$$\nabla\nabla^T f = \begin{pmatrix} -2 & -2 \\ -2 & -2 \end{pmatrix}.$$

The two normalized eigenvectors of $\nabla\nabla^T f$ are

$$\vec{v}_1 = \begin{pmatrix} 1/\sqrt{2} \\ 1/\sqrt{2} \end{pmatrix} \text{ and } \vec{v}_2 = \begin{pmatrix} 1/\sqrt{2} \\ -1/\sqrt{2} \end{pmatrix},$$

with eigenvalues -4 and 0. Note that ∇f can be re-expressed more clearly as $\nabla f = 2\sqrt{2}[1 - (x+y)]\vec{v}_1 + 0\vec{v}_2$. Now

$$\nabla\nabla^T f = -4\vec{v}_1\vec{v}_1^T + 0\vec{v}_2\vec{v}_2^T. \tag{B3}$$

Let

$$\underline{M} = \nabla\nabla^T f - \vec{v}_2\vec{v}_2^T = -4\vec{v}_1\vec{v}_1^T - \vec{v}_2\vec{v}_2^T. \tag{B4}$$

Clearly,

$$\underline{M}^{-1} = -\tfrac{1}{4}\vec{v}_1\vec{v}_1^T - \vec{v}_2\vec{v}_2^T. \tag{B5}$$

Now let

$$\underline{V} = \underline{M}^{-1} + \vec{v}_2\vec{v}_2^T = -\tfrac{1}{4}\vec{v}_1\vec{v}_1^T$$

$$= -\frac{1}{4}\begin{pmatrix} \frac{1}{2} & \frac{1}{2} \\ \frac{1}{2} & \frac{1}{2} \end{pmatrix} = -\frac{1}{8}\begin{pmatrix} 1 & 1 \\ 1 & 1 \end{pmatrix}. \tag{B6}$$

Assume a starting value x_0, y_0. Then the first step is

$$-\underline{V}\cdot\nabla F_0 = +\frac{1}{8}\begin{pmatrix} 1 & 1 \\ 1 & 1 \end{pmatrix}\cdot 2[1 - (x_0 + y_0)]\begin{pmatrix} 1 \\ 1 \end{pmatrix}$$

$$= \frac{1}{2}\begin{pmatrix} 1 - (x_0+y_0) \\ 1 - (x_0+y_0) \end{pmatrix}.$$

Thus

$$\begin{pmatrix} x_1 \\ y_1 \end{pmatrix} = \begin{pmatrix} x_0 \\ y_0 \end{pmatrix} - \underline{V}\cdot\nabla F_0 \tag{B7}$$

$$= \begin{pmatrix} \frac{1}{2} \\ \frac{1}{2} \end{pmatrix} + \begin{pmatrix} \frac{x_0 - y_0}{2} \\ \frac{y_0 - x_0}{2} \end{pmatrix}, \tag{B8}$$

$$x_1 + y_1 = \frac{1}{2} + \frac{x_0 - y_0}{2} + \frac{1}{2} - \frac{x_0 - y_0}{2} = 1,$$

and we are at the minimum in one step, as we should be since F is quadratic.

Thus the problem in a multidimensional case reduces to finding the eigenvectors with zero eigenvalues, subtracting the rank-one matrices generated by these eigenvectors, inverting the resulting matrix, and finally adding back the rank-one subtractions.

In the case of likelihood problems such as ours, the eigenvector for scale changes is $\vec{A}$ and the eigenvector for phase changes is $i\vec{A}$. Thus we automatically had the necessary two eigenvectors.

APPENDIX C: CHOICE OF ANGULAR MOMENTUM BARRIER FACTORS AND OF THE N^* RADIUS

Unfortunately three different forms of barrier-penetration factors $B_L(QR)$ are now common in partial-wave analyses. This appendix compares them in Fig. 17, points out that for $L \geq 2$ they may differ, and makes a plea for using the standard Blatt-Weisskopf factors, which have recently been given considerable support by von Hippel and Quigg.[39]

In the text, Eq. (3.10), we used the notation $b_{L'}$ for the barrier factor for the amplitude T; here we use the more standard notation B_L ($= |b_{L'}|^2$) for the barrier factor for the intensity $|T|^2$. The "industry standard" for B_L is taken from Eq. (5–8), page 361, of Blatt and Weisskopf[21] (where they are called v_l),

$$B_0 = 1, \quad B_1 = \frac{x^2}{1+x^2}, \quad B_2 = \frac{x^4}{9+3x^2+x^4}, \ldots, \tag{C1}$$

where $x = QR$. These B_L have the property that their inflection point is at about $QR = L$. For $x \ll L$, they start off as

$$B_L \xrightarrow[x \to 0]{} \frac{x^{2L}}{[(2L-1)!!]^2}, \tag{C2}$$

and for $x \gg L$, $B_L \to 1$. Figure 17 gives B_L vs QR for $L = 1$ to 7.

There is general agreement that the B_L should start out as x^{2L} and should approach unity for large L; but before the 1972 paper of von Hippel and Quigg,[39] the detailed form (C1) was regarded with some skepticism by particle physicists because it was derived by assuming that the region of interaction was a square well. This is reasonable when the intermediate state is a nucleus, which is what Blatt and Weisskopf had in mind, but less convincing when it is an N^*. Accordingly, many physicists just used the low-QR form (C2), or perhaps a form somewhat like that for $L = 1$, which has the correct limiting properties at both ends

$$B_L \approx \frac{x^{2L}}{\text{const} + x^{2L}}, \tag{C3}$$

but in general does not have its inflection point near $QR = L$. von Hippel and Quigg have now shown that form (C1) can be rederived using only the properties of the radial wave function $U_L(x) \propto x h_L(x)$, where h_L is a Hankel function. For more discussion and an approximate form, see Ref. 40.

Figure 17 shows not only the Blatt-Weisskopf form of B_L, but the small-QR approximation for $L = 1$ to 3. As one expects, both approximations fail badly by $QR = L$. This brings us to our proposal. Now that the Blatt-Weisskopf form has been well justified, why not use it? Then, once most analyses use the same barrier, we can go on to gather experience on the best value for the radius R.

Next we take up the question of what value to choose for the radius parameter R. Barbaro-Galtieri[41] has done a thorough analysis of the $\Delta(1336)$ peak and finds that R should be about 1 F. Yet when R is used in a far more indirect way to do SU(3) fits, it turns out that values of 0.2 F,[41] or even zero,[42] work best.

The radius question, specifically as it applies

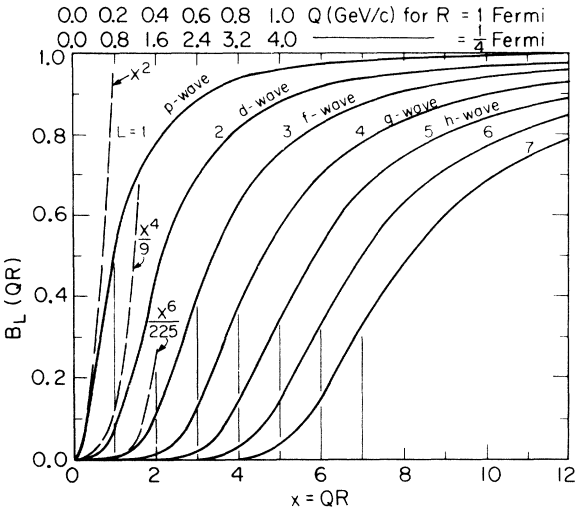

FIG. 17. Blatt-Weisskopf barriers [Eq. (C1)] for $L = 1$ through 7, compared with their approximate forms [Eq. (C2)] for low QR.

to our reaction $\pi N \to \pi\pi N$, has recently been studied at Saclay by Dolbeau[43] in his isobar analysis in the $\sqrt{s}$ range 1390–1740 MeV. These fits are very sensitive to the radius, particularly near ρ threshold around 1700 MeV. Dolbeau finds a best radius of $\sim\frac{1}{4}$ F, i.e., in between the large value favored by the $\Delta(1236)$ and the small value favored by SU(3). Specifically he finds that $1/R$ should be 750 ± 250 MeV/c.

Finally a comment on what we ourselves did. Because of a programming mistake, we started our fits using the small-QR approximation (C2), and did not catch the mistake until so late that it was expensive to refit. But now Dolbeau's finding that the best value of R is only $\frac{1}{4}$ F keeps QR so low that it does not pay for us to refit. Specifically, consider the kinematics of our reaction even at our highest energy $\sqrt{s} = 1970$ MeV, and set $R = \frac{1}{750}$ MeV/c. Then for

$$\pi N \to \Delta(1236)\pi, \quad Q_\Delta = Q_\pi \equiv Q = 393 \text{ MeV}/c, \quad QR = 0.52,$$

$$\to \rho(770)N, \quad Q_\rho = Q_N \equiv Q = 500 \text{ MeV}/c, \quad QR = 0.67.$$

This means that near the resonance bands of our Dalitz plots, where we find most of our data, the small-QR approximation is quite good, and we have decided not to refit. In our K-matrix programs for energy-dependent fits we have always used the standard Blatt-Weisskopf form (C1).

*Work supported by the U. S. Atomic Energy Commission.

†Present address: Lawrence Livermore Laboratory, Livermore, California 94550.

‡Present address: CEN, Saclay, France.

§Present address: DESY, Notkestieg 1, 2000 Hamburg-52.

‖Present address: Nuclear Physics Laboratory, Oxford, OX1-3RH.

[1]S. Almehed and C. Lovelace, Nucl. Phys. B40, 157 (1972). For earlier references, see our Ref. 3.

[2]R. Ayed and P. Bareyre, paper presented at the Second International Conference on Elementary Particles, Aix-en-Provence, 1973 (unpublished).

[3]Particle Data Group, Rev. Mod. Phys. 45, S1 (1973).

[4]A. D. Brody *et al.*, Phys. Lett. 34B, 665 (1971).

[5]U. Mehtani *et al.*, Phys. Rev. Lett. 29, 1634 (1972); Y. Williamson *et al.*, *ibid.* 29, 1353 (1972); A. Kernan *et al.*, in *Baryon Resonances—73*, proceedings of the Purdue Conference on Baryon Resonances, edited by E. C. Fowler (Purdue Univ. Press, Lafayette, Indiana, 1973), p. 113.

[6]P. Eberhard and M. Pripstein, Phys. Rev. Lett. 10, 8 (1963).

[7]B. Deler *et al.*, Nuovo Cimento 45A, 559 (1966).

[8]M. DeBeer *et al.*, Nucl. Phys. B12, 599 (1969); B12, 617 (1969). Further analyses may be found in the theses of B. Deler [CEA-R-3579, 1969 (unpublished)]; G. Smadja [Orsay Series A, No. 556, 1969 (unpublished)], M. P. Chavannon [D. Ph. P. E. Saclay, 1971 (unpublished)], Nguyen Thuc Diem [CEA-N-1602, 1973 (unpublished)]; in the recent papers by J. Dolbeau and F. Triantis, paper submitted to the Second International Conference on Elementary Particles, Aix-en-Provence, 1973 (unpublished); P. Chavannon, J. Dolbeau, and G. Smadja, Nucl. Phys. B75, 157 (1974); J. Dolbeau, M. Neveu, F. A. Triantis, and C. Coutures, *ibid.* B78, 233 (1974).

[9]M. G. Bowler and R. J. Cashmore, Nucl. Phys. B17, 331 (1970).

[10]W. Chinowsky, J. M. Mulvey, and D. H. Saxon, Phys. Phys. Rev. D 2, 1790 (1970).

[11]D. J. Herndon *et al.*, LBL Report No. LBL-1065/SLAC-PUB-1108, presented to the XVI International Conference on High Energy Physics, Chicago-Batavia, Ill., 1972 (unpublished).

[12]A. D. Brody *et al.*, Phys. Rev. D 4, 2693 (1971).

[13]U. C. Riverside-LBL collaboration; see U. Mehtani *et al.* and Y. Williamson *et al.*, Ref. 5.

[14]D. J. Herndon, P. Söding, and R. J. Cashmore, preceding paper, Phys. Rev. D 11, 3165 (1975).

[15]G. Smadja, LBL Report No. LBL-382, 1974 (unpublished). We have found a mistake in this paper which greatly underestimates the problem.

[16]R. Aaron and R. D. Amado, Phys. Rev. Lett. 31, 1157 (1973); G. Gustafson, Nucl. Phys. B63, 325 (1973).

[17]The preliminary conclusions of R. Ascoli (private communication, 1974) are that the corrections will not be very significant.

[18]Y. N. Goradia, T. A. Lasinski, G. Smadja, and M. Tabak, LBL Report No. LBL-3011, 1974 (unpublished).

[19]S. D. Protopopescu *et al.*, Phys. Rev. D 7, 1279 (1973); B. Hyams *et al.*, Nucl. Phys. B64, 134 (1973); P. Baillon *et al.*, Phys. Lett. 38B, 555 (1972).

[20]D. J. Herndon, Ph.D. thesis, University of California, Berkeley, 1972, LBL Report No. LBL-544, 1972 (unpublished).

[21]J. Blatt and V. F. Weisskopf, *Theoretical Nuclear Physics* (Wiley, New York, 1952).

[22]In our case, four kinematic variables are needed for each event: two Dalitz plot variables, and two angles, θ and ϕ. The Dalitz plots of Figs. 2–4 require 10–100 bins. The cosθ distributions of Fig. 5 need ~ 20 bins and the ϕ distribution needs another 10 bins. The total number of bins is then ~ 2000–$20\,000$, while the experiment has only $\sim 10\,000$ events at each momentum. Under these circumstances, the event population in each bin would be too small to allow the assumption of a Gaussian distribution. It follows that the maximum-likelihood technique would be the most appropriate fitting method to apply in our experiment.

[23]L. R. Miller, Ph.D. thesis, University of California, Berkeley, LBL Report No. LBL-38, 1974 (unpublished).

[24]F. T. Solmitz, Ann. Rev. Nucl. Sci. 14, 379 (1964), Eq. (36).

[25]W. C. Davidon, Computer J. 10, 406 (1967).

[26]P. Eberhard and W. O. Koellner, LBL Report No. UCRL-20159, 1970 (unpublished).

[27]P. H. Eberhard, A. H. Rosenfeld, and M. Tabak, Group A Memo (private communication, 1974).

[28]Some of the numbers and conclusions in this paragraph differ from those of Miller's thesis (Ref. 23), which we now think are wrong.

[29]Eventually.

[30]D. Faiman and J. Rosner, Phys. Lett. 45B, 357 (1973). We gratefully acknowledge the help of David Faiman, who suggested the four new amplitudes which led to the discovery of solution B.

[31]E. Flaminio, J. D. Hansen, D. R. O. Morrison, and N. Tovey, CERN-HERA Reports Nos. 70-4 and 70-7, 1970 (unpublished).

[32]R. Longacre, Ph.D. thesis, University of California, Berkeley, 1973, LBL Report No. LBL-948, 1974 (unpublished); R. Longacre *et al.*, LBL Report No. LBL-2636/SLAC-PUB-1389 (unpublished).

[33]R. H. Dalitz, in πN *Scattering*, proceedings of the Conference on πN Scattering, Irvine, California, 1967, edited by G. L. Shaw and D. Y. Wong (Wiley-Interscience, New York, 1969), p. 187.

[34]F. J. Gilman, M. Kugler, and S. Meskov, Phys. Lett. 45B, 481 (1973); Phys. Rev. D 9, 715 (1974).

[35]R. J. Cashmore, in *Baryon Resonances—1973*, proceedings of the Purdue Conference on Baryon Resonances, edited by E. C. Fowler (Purdue Univ. Press, Lafayette, Indiana, 1973), p. 53.

[36]A. H. Rosenfeld, in Lectures at the International School of Subnuclear Physics, Erice, Sicily, 1973 (unpublished); LBL Report No. LBL-2098 (unpublished).

[37]R. J. Cashmore, D. W. G. S. Leith, R. S. Longacre, and A. H. Rosenfeld, LBL Report No. LBL-2635/SLAC-PUB-1388, 1974 (unpublished).

[38]R. S. Longacre *et al.*, Phys. Lett. 55B, 415 (1975).

[39]F. von Hippel and C. Quigg, Phys. Rev. D 5, 624 (1972).

[40]A. H. Rosenfeld, in *Particle Physics*, proceedings of the Irvine conference on Particle Physics, 1971, edited by M. Bander, G. L. Shaw, and D. Y. Wong (A.I.P., New York, 1972).

[41]A. Barbaro-Galtieri, in *Properties of the Fundamental Interactions*, proceedings of the 1971 International

Summer School "Ettore Majorana," Erice, Italy, 1971, edited by A. Zichichi (Editrice Compositori, Bologna, 1973); LBL Report No. LBL-555 (unpublished). See particularly Table V.

[42]D. E. Plane *et al.*, Nucl. Phys. B22, 93 (1970).

[43]J. Dolbeau, Ph.D. thesis, 1974, D. Ph. P. E., Saclay (unpublished).

[44]D. J. Herndon *et al.*, supplement to LBL Report No. LBL 1065 (Rev.), 1974 (unpublished) or SLAC Report No. SLAC-PUB-1108, 1974 (unpublished).

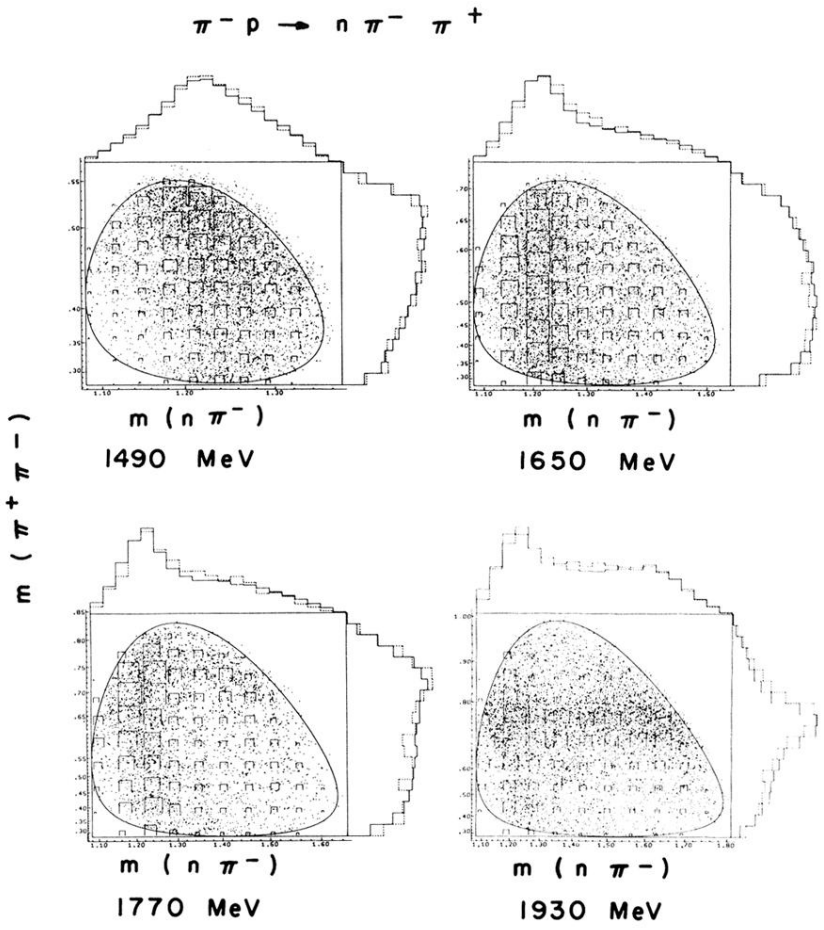

FIG. 2. Dalitz plots for the state $n\pi^-\pi^+$ at four c.m. energies: 1490, 1650, 1770, and 1930 MeV. The side of the little squares is proportional to the predicted density of our fits. On the projected distributions, the dotted line is the experimental data, while the solid histogram is the result of the fit. The scales are linear in $(\text{mass})^2$, but the tiny numbers are actually in MeV.

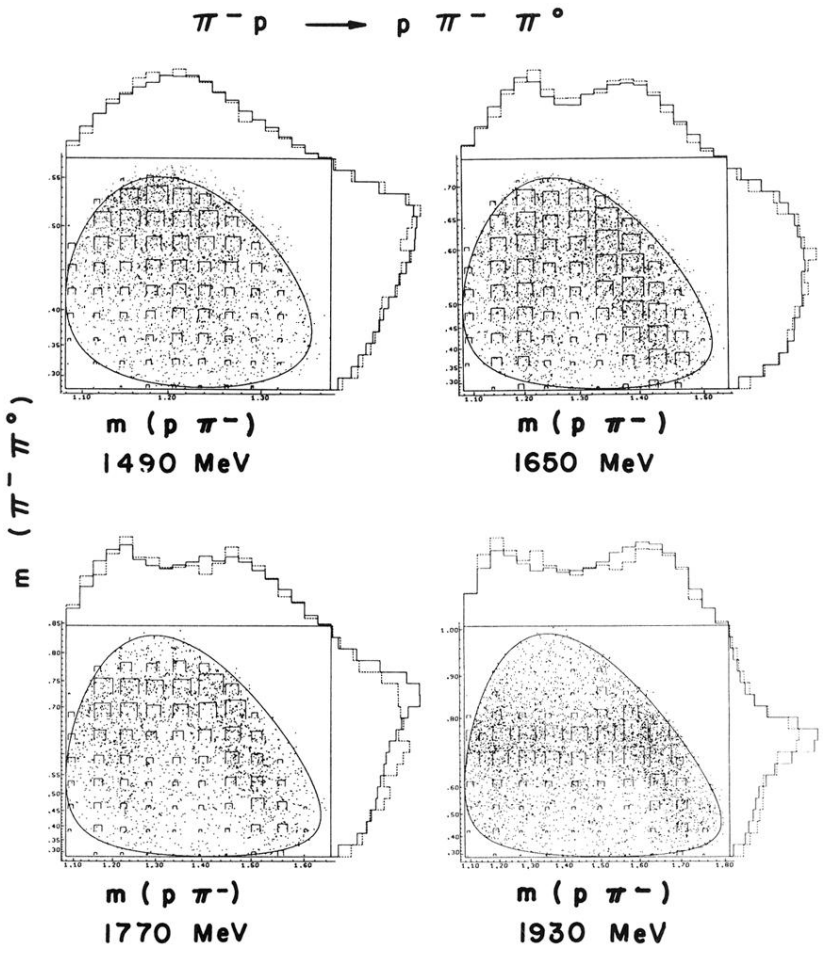

FIG. 3. Dalitz plot for the state $p\pi^-\pi^0$. For details see caption to Fig. 2.

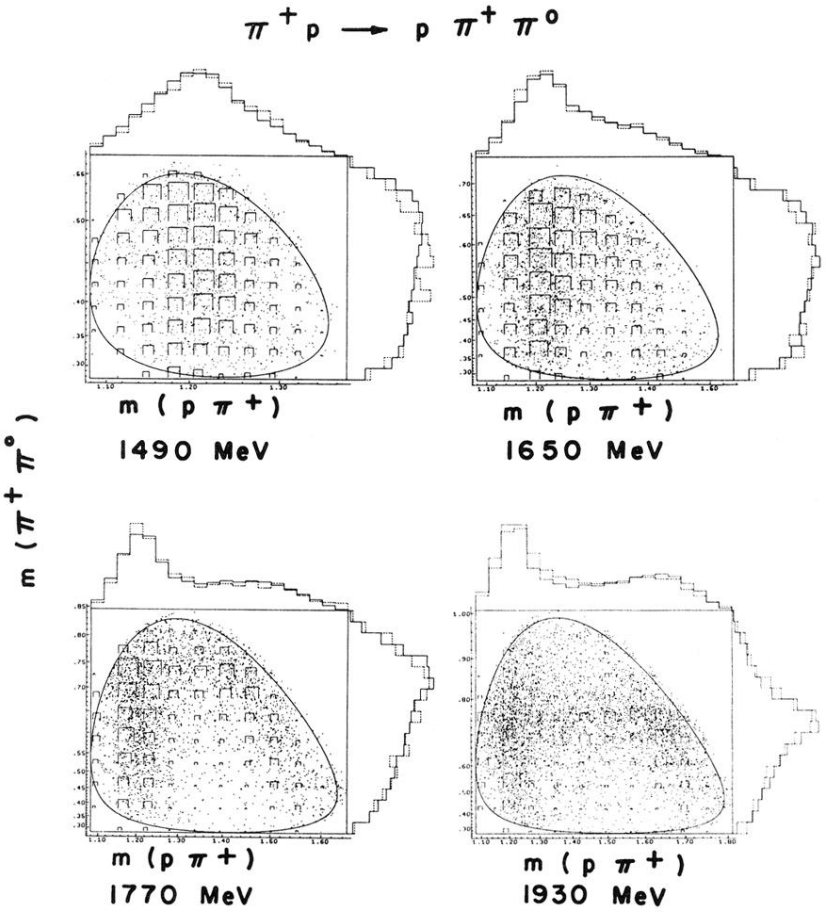

FIG. 4. Dalitz plot for the state $p\pi^+\pi^0$. For details see caption to Fig. 2.